Magnetization of exsolution intergrowths of hematite and ilmenite: Mineral chemistry, phase relations, and magnetic properties of hemo-ilmenite ores with micron- to nanometer-scale lamellae from Allard Lake, Quebec

Suzanne A. McEnroe,[1] Peter Robinson,[1,2] Falko Langenhorst,[3,4] Cathrine Frandsen,[5] Michael P. Terry,[3] and Tiziana Boffa Ballaran[3]

[1]   Hemo-ilmenite ores from Allard Lake, Quebec, were first studied over 50 years ago. Interest was renewed in these coarsely exsolved oxides, based on the theory of lamellar magnetism as an explanation for the high and stable natural remanent magnetizations (NRMs), 32 to 120 A/m, reported here. To understand the magnetism and evolution of the exsolution lamellae, the microstructures and nanostructures were studied using scanning electron microscopy and transmission electron microscopy (TEM), phase chemistry, and relations between mineral chemistry and the hematite-ilmenite phase diagram. Cycles of exsolution during slow cooling resulted in lamellae down to $1-2$ nm thick. Combined electron microprobe, TEM, and X-ray diffraction (XRD) results indicate that hematite hosts reached a composition approximately ilmenite (Ilm) 14.4, and ilmenite hosts $\sim$Ilm 98. The bulk of the very stable NRM, which shows thermal unblocking $\sim595-620°C$, was acquired during final exsolution in the two-phase region canted antiferromagnetic $R\bar{3}c$ hematite $+ R\bar{3}$ ilmenite. Hysteresis measurements show a very strong anisotropy, with a stronger coercivity normal to, than parallel to, the basal plane orientation of the lamellae. Magnetic saturation (M_s) values are up to 914 A/m, compared to 564 A/m predicted for a modally equivalent spin-canted hematite corrected for $\sim15\%$ $R^{2+}TiO_3$ substitution. Low-temperature hysteresis, AC-susceptibility measurements, and Mössbauer results indicate a Néel temperature (T_N) of the geikielite-substituted ilmenite at $\sim$43 K. The low-temperature hysteresis and AC-susceptibility measurements also show a cluster-spin-glass-like transition near 20 K. Below T_N of ilmenite an exchange bias occurs with a 40 mT shift at 10 K.

1.   Introduction

[2]   The hemo-ilmenite ores from the Allard Lake area, Quebec, have been of interest for their magnetic properties since the 1950s [*Hargraves*, 1959a; *Carmichael*, 1961]. Nearly 50 years later, Hargraves' interest was rekindled in these rocks with the discovery of magnetic anomalies on Mars and with the concept of lamellar magnetism [*Robinson et al.*, 2002, 2004]. Because the hemo-ilmenite ore bodies produce large remanent magnetic anomalies, these are possible analog rocks for the Martian magnetic anomalies.

[3]   For the Allard Lake ore samples, some authors favored a magnetization carried by large multidomain lamellae of hematite formed and magnetized at high temperature [*Kletetschka et al.*, 2002] but failed to take the ilmenite-hematite phase diagram into account properly. Thermoremanent magnetization (TRM) experiments [*Carmichael*, 1961; R. B. Hargraves, unpublished data, 2002] showed the TRM of Allard Lake samples is <50% of the original natural remanent magnetization (NRM), supporting a chemical remanent magnetization (CRM) mechanism, related to lamellar formation, for the NRM. Here we explore the nature of the phase diagram, the role of exsolution and the temperatures (T) of exsolution, especially in relation to the acquisition of magnetization.

[4]   To gain a greater understanding of the physical, chemical, and magnetic properties of Allard Lake hemo-ilmenite, we undertook a concentrated study on samples

---

[1]Geological Survey of Norway, Trondheim, Norway.
[2]Also at Department of Geosciences, University of Massachusetts, Amherst, Massachusetts, USA.
[3]Bayerisches Geoinstitut, Universität Bayreuth, Bayreuth, Germany.
[4]Institute of Geosciences, Friedrich-Schiller-University Jena, Jena, Germany.
[5]Department of Physics, Technical University of Denmark, Kongens Lyngby, Denmark.

AL23b and AL36b from the Lac Tio deposit, using scanning electron microscopy (SEM) and transmission electron microscopy (TEM) images, electron microprobe (EMP) and TEM chemical analyses, powder X-ray diffraction, Mössbauer spectroscopy, and high- and low-temperature magnetic experiments. Sample AL36b was chosen particularly because all evidence showed it is free of magnetite that does occur in many Allard Lake samples, and would thus yield clear information on properties purely related to the hematite-ilmenite solid solution. Magnetic data on samples AL20c, AL114, and AL46 from Lac Tio and AL7b from Lac Ellen are also reported.

2. Characteristics of the Allard Lake Deposits

[5] The massive hemo-ilmenite deposits in the Allard Lake region of the Mesoproterozoic Grenville Province of Canada have been known since the early 1940s. The aeromagnetic survey was one of the first ever made to explore for an ore deposit. The large negative aeromagnetic anomaly over the main Lac Tio ore body is more than 5000 nT below background, at a flying height of 500 feet [*Bourret*, 1949], and is dominated by the reversed magnetic remanence in the ore. Later ground magnetic surveys and dip needle measurements confirmed the magnetic orientation of the ilmenite ore as opposite to that of the present-day magnetic field [*Bourret*, 1949; *Hammond*, 1952]. The remanent magnetization was first characterized in detail by *Carmichael* [1959, 1961, 1964] and *Hargraves* [1959a]. Because the concept of plate tectonics had not yet been invented, nor were reversals of Earth's magnetic field understood, early exploration for these deposits was a conceptual challenge that was met successfully. The Lac Tio ore was, and is still, the largest massive ilmenite deposit mined in the world today. It has produced tens of millions of tons of hemo-ilmenite and has a resource exceeding 180 million tons [*Stanaway*, 2005].

[6] *Hargraves* [1959a, 1962] established the following paragenetic sequence on the basis of field and petrographic evidence, from oldest to youngest: anorthosite, oxide-rich norite, hemo-ilmenite ores, and syenite. Recent petrologic studies in related regions suggest the oxide-rich rocks are cumulates precipitated from plagioclase-rich magmas [*Ashwal*, 1993]. The ores contain >85% hemo-ilmenite, the remainder being plagioclase ± minor to rare pyrite, pyrrhotite and magnetite. The samples in these early studies, and new samples sent from Rio Tinto Ltd., show strong and stable NRMs. Samples reported by R. B. Hargraves (Table 1) and here have NRM intensities from 12 to 120 A/m. The ores are characterized by a very hard magnetization (Figure 1) with the bulk of the NRM retained after alternating field demagnetization to 120 mT and to T above 600°C [*Hargraves*, 1959a; *Hargraves and Burt*, 1967; *Carmichael*, 1961]. Samples with magnetite start to unblock at lower temperatures but usually have a high-temperature component.

[7] Key aspects of understanding the magnetism of the Lac Tio hemo-ilmenites came from *Hargraves'* [1959a] understanding of two magnetic properties of hemo-ilmenite crystals: (1) that the magnetization is located in or close to the basal (0001) plane, and (2) there is a strong anisotropy of magnetic susceptibility (AMS), such that the susceptibility is strongest parallel to the basal plane (k1−k2) and weakest parallel to the crystallographic **c** axis (k3). *Hargraves* [1959a] used measurements of the AMS to show that the hemo-ilmenite ores have a moderate to strong lattice-preferred orientation, with statistical basal planes oriented apparently parallel to the irregular basal contact of the ore body, and geographically at various angles to the estimated Mesoproterozoic magnetizing field. This prevented NRM of most samples from being oriented parallel to the field, but to lie as close to the field vector as the dominant crystal directions would allow. Using the results of AMS orientation data, and magnetization orientation data, he devised a graphical approach to determine the field direction. These results were in agreement with magnetizing field orientations determined by standard techniques for other rocks in the district [*Hargraves and Burt*, 1967].

[8] This work later became one aspect of the lamellar magnetism hypothesis and the external force concept (see below) [*Robinson et al.*, 2002, 2004]. This showed that the intensity of magnetization is generally greatest in samples where the statistical basal plane, (0001), is nearly parallel to the magnetizing field, v, thus the smallest (0001) ^ v [angle of (0001) to v] as in Table 1, and least when the statistical basal plane is nearly perpendicular to the magnetizing field. This geometrical relationship may also be true for TRM of hematite, and is not special to lamellar magnetism. AMS results and positioning of the statistical basal plane are hampered geometrically in samples with magnetite (highest susceptibilities in Table 1), and less reliable in samples with a weak anisotropy factor, indicated by Hargraves as the ratio of the longest to the shortest axis (k1/k3) of the anisotropy ellipsoid.

[9] Samples reported by Hargraves have NRM intensities from 12 to 119 A/m (our smaller data set has 32 to 120 A/m, reported later). Table 1 shows representative data on 22 selected out of Hargraves larger collection of 57. Selection was based on obtaining 5 or 6 largest (h) and smallest (s) values for each of four properties: NRM, anisotropy factor [k1/k3], angle of the statistical (0001) basal plane to the magnetizing field [(0001) ^ v], and susceptibility. Data are arranged in order of NRM, 6 high values (h), 11 middle values (m), and 5 small values (s). Susceptibilities data (SI units) are in three groups: 8 s values, $2.5-8.7 \times 10^{-3}$; 4 m values, $17-23 \times 10^{-3}$; and 10 h values, $29-110 \times 10^{-3}$. The h group may have up to ~3% magnetite. A key observation in Table 1 is that five out of six samples with highest NRM values have the lowest susceptibilities and lack magnetite.

[10] The anisotropy factor [k1/k3] ranges from 3.68 to 1.22. Of the six samples with the highest anisotropy (h), 3.68−2.85, four are in susceptibility group m, and four are in h. Samples with the highest NRMs and low susceptibility, have lower anisotropies, 2.66−1.48. The 10 samples with highest susceptibility (h) have highly varied anisotropies, 3.60−1.35. Possibly for the high-anisotropy samples, with medium susceptibilities, the small amounts of magnetite have a shape orientation tied to the ilmenite fabric, which enhances the magnetic anisotropy, not observed for samples with low susceptibility. The correlation between NRM intensity and (0001) ^ v shown in the larger collection [*Robinson et al.*, 2004; P. Robinson and S. A. McEnroe, manuscript in preparation, 2007] is less obvious here, where
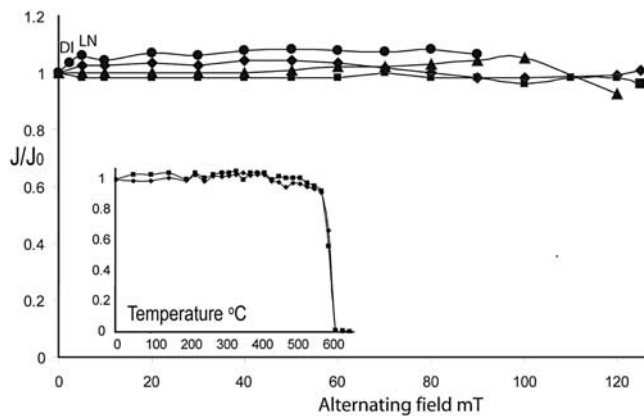
Figure 1. Alternating field demagnetization curves of Allard Lake hemo-ilmenite samples to a maximum field of 140 mT. Sample AL114 (circle) was first LTD by cooling in dry ice (DI) and liquid nitrogen (LN) with only a slight increase in magnetization noted. Inset shows thermal demagnetization curves. In thermal demagnetization in samples with or without minor magnetite, major unblocking occurs at $600–610°C$, well above the $570–580°C$ unblocking T of magnetite.

point-counted mode, 29.5% of the grains are composed of optically visible hematite lamellae. The largest first-generation lamellae are ~40 μm thick. These contain finer ilmenite exsolution down to the optical limit of the microscope (~0.2 μm). Second generation hematite lamellae are also visible in the ilmenite host. In SEM images these small hematite lamellae are shown to have ilmenite lamellae. Magnetite, rutile needles, discrete pyrite and pyrrhotite are also present in AL20c. A late stage alteration with magnetite replacing hematite is commonly associated with sulfides. Magnetite is present also as elongate plates replacing some hematite. These alterations and accessory phases are reported from different parts of the Lac Tio deposit [*Hammond*, 1952; *Hargraves*, 1959a]. Interestingly, samples with magnetite typically have NRM values lower than the samples without magnetite (Table 1).

[13] TEM images of ilmenite and hematite of AL 23b and AL36b are very similar. These show a stranded microstructure with various generations of exsolution, some beyond the resolution of SEM. Figure 3a shows an ilmenite host with tiny (<20 nm) and medium-sized (0.5 μm) hematite exsolutions. Host ilmenite and exsolved hematite are in epitactic orientation relationship, whereby the **a** and **c** axes of both are parallel to each other. The nanometer-sized

angles of the six high-NRM samples range from $1.3°$ to $58.6°$. The key samples studied here, AL36b, AL7b, and AL23b (companion sample to AL23c in Table 1), have moderate to very strong NRM, low susceptibility, relatively weak anisotropy and statistical basal planes at a moderate to large angle from the magnetizing field.

[11] Though previous workers had studied this deposit, questions remained concerning the type of magnetization, a CRM or a TRM, the origin of the very high coercivity, and the interplay between chemical and magnetic interactions at different compositions and temperatures that are important in the acquisition of magnetization. With new insights into the mechanism of magnetization caused by a defect moment at the lamellar interfaces, termed lamellar magnetism [*Robinson et al.*, 2002, 2004], this deposit became a primary target to evaluate the magnetic effects of the lamellar interfaces. The aim of this paper is to explore some of the long-standing questions about the origin of magnetization of the ore that has the stability and intensity to produce anomalies of a magnitude needed for those measured on Mars. In organizing this paper, we have chosen to present all of the physical and chemical data, as well as theoretical information and phase diagrams first, followed by information on magnetic properties and their interpretation.

3. Exsolution Microstructures

[12] *Hargraves* [1959a] and *Carmichael* [1961] showed the many scales of exsolution lamellae at the optical scale [see also *Robinson et al.*, 2004]. We further characterized samples AL7b, AL20c, AL23b, and AL36b by optical microscopy, and by scanning electron microscope (SEM). Samples consist (Figure 2) of ilmenite host grains (darker) with large hematite exsolution lamellae (lighter) parallel to (0001), and with second and subsequent generations of hematite lamellae also parallel to (0001). In a typical

Table 1. Selected Magnetic Property Data of *Hargraves* [1959a] on Representative Samples From the Lac Tio and Lac Ellen Hemo-ilmenite Deposits[a]

Sample	NRM[b]	NRM[c]	k1/k3[d]	(0001)[e] $\wedge$ v[f]	Susceptibility[g]
7b	118.5 h		1.48 s	58.6 m	0.002979 s
71b	112.2 h		1.85 m	53.8 m	0.003016 s
7a	103 h	95 h	1.50 s	52.4 m	0.002514 s
26b	88.3 h	91.2 h	1.83 m	1.3 s	0.006724 s
214a	85.4 h		2.66 m	4.7 s	0.038961 h
23c	80.1 h	93.4 h	1.68 m	24.1 s	0.004977 s
110a	56.4 m		2.87 h	48.0 m	0.036322 h
20c	51.4 m		1.40 s	22.7 s	0.052284 h
210b	51.4 m		3.68 h	15.6 s	0.021868 m
85a	49.3 m		3.11 h	34.5 m	0.022874 m
90a	46.2 m		1.79 m	64.2 m	0.104691 h
95c	46.2 m		2.03 m	54.2 m	0.051780 h
97b	44.1 m		2.21 m	83.1 h	0.109719 h
216b	44.1 m		1.25 s	32.6 m	0.008735 s
114b	41.1 m		2.85 h	51.6 m	0.017721 m
206a	40 m		2.89 h	19.8 s	0.016967 m
46b	31.8 m		1.35 s	31.1 m	0.045999 h
36b	22.5 s		1.22 s	73.9 h	0.003293 s
36a	18.4 s		1.56 m	82.8 h	0.002966 s
207a	17.4 s		2.38 m	34.8 m	0.042354 h
213b	15.5 s		1.89 m	79.0 h	0.029409 h
112a	12.6 s	11.6 s	3.60 h	75.1 h	0.044742 h

[a]Listed in order of NRM intensity. From lists of data on 57 samples, 51 from Lac Tio from *Hargraves* [1959a] and 6 from Lac Ellen from *Hargraves* [1959b]. The lowercase letters "h," "m," and "s" refer to high, medium, and small values within each property list.
[b]A/m, based on a linear correlation of ten 1959 data points and ten modern data points, $y = 10 (1.324 \times -5.257)$, where y is corrected value and x is old value.
[c]R. B. Hargraves (personal communication, 2002) for the 1980s.
[d]AMS anisotropy factor, k1/k3 is ratio of long to short axis of AMS ellipsoid.
[e]The statistical (0001) plane of lattice-preferred orientation, which is normal to the k3 axis of the AMS ellipsoid.
[f]Vector of reversed magnetizing field inverted into the lower hemisphere at declination 47.9, inclination 83.3.
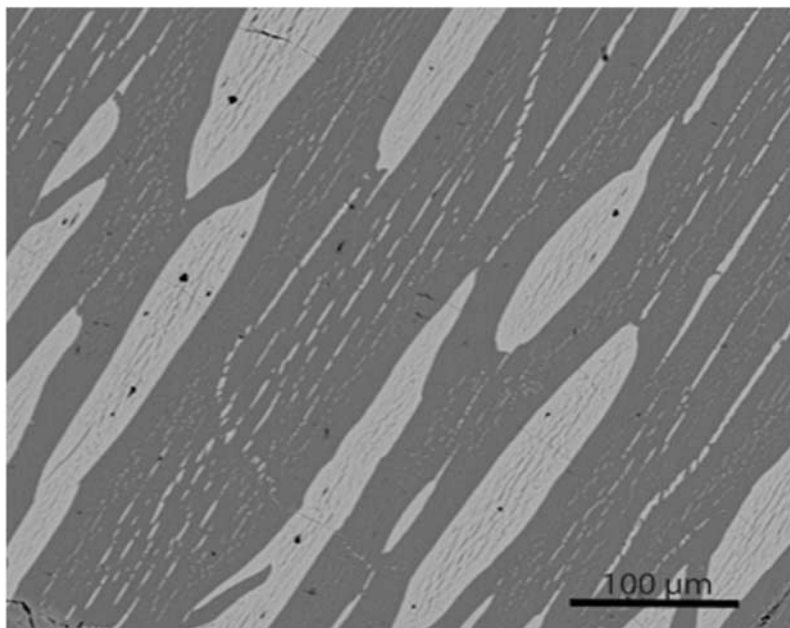[g]Susceptibility SI converted from Hargraves values in emu.

Figure 2. SEM electron backscatter image of coarsely exsolved hemo-ilmenite sample AL36b from Allard Lake. Ilmenite host grains (darker) with large hematite exsolution lamellae (lighter) parallel to (0001) and with second and subsequent generations of hematite lamellae also parallel to (0001). The largest first-generation lamellae are $\sim$40 μm thick. These contain finer ilmenite exsolution down to the optical limit of the microscope ($\sim$0.2 μm). Second generation hematite lamellae are also visible in the ilmenite host. These are generally free of optically visible ilmenite.

hematite lenses are present particularly in the middle of ilmenite regions where larger hematite exsolutions are relatively widely spaced. As is typical for a stranded microstructure reflecting a stranded diffusion profile, these tiniest hematite exsolutions are absent in ilmenite regions directly adjacent to large hematite exsolution lamellae.

[14] Figure 3b shows a large hematite exsolution lamella (to right) more than 5 μm wide in an ilmenite host. These, as well as medium-sized exsolutions ($\sim$0.5 μm), contain numerous misfit dislocations at the interface to the surrounding host phase. The smallest and hence latest exsolutions are tiny ilmenite lenses a few nanometers thick within hematite. These are fully coherent with the surrounding host lattice and hence are not decorated with misfit dislocations. However, they are surrounded by shadows of strain contrast. Unlike the areas of ilmenite host described above, fine ilmenite lamellae within the coarse hematite lamellae seem to be abundant throughout, except within a few nm of contacts of coarse ilmenite, where the hematite has developed a very fine scale mottling, indicative of chemical heterogeneity on a unit cell length scale. This is consistent with analytical results given below, where lamellar-free areas along boundaries of ilmenite against hematite have been found and analyzed by electron microprobe, but such areas have not been located within hematite along boundaries with ilmenite.

4. Chemical Analyses by Electron Microprobe Probe and TEM-EDX

[15] Electron microprobe (EMP) analyses were performed at Bayerisches Geoinstitut, University of Bayreuth, on three Allard Lake samples, AL7b from Lac Ellen, and AL23b and AL36b, both from the Lac Tio Deposit. AL23b and AL7b analyses were made on a Jeol microprobe, and AL36b on a Cameca microprobe. Weight% analyses of the oxides (Table 2), with Fe analyzed as FeO, were converted to stoichiometric formulae based on 2 cations and 3 oxygens, with necessary added oxygens used for partial conversion of Fe^{2+} to Fe^{3+} and FeO to Fe_2O_3. Formulations are also expressed in terms of mole% of end-members or major component ratios, shown either as mole fraction in figures or mol % throughout the text. The key ratios are "Ilm" = $R^{2+}TiO_3/(R^{2+}TiO_3 + R^{3+}_2O_3)$ (R^{2+} = all divalent cations and R^{3+} = all trivalent cations), also calculated more simply as $2Ti/(2Ti + R^{3+})$ and "Geik" = $MgTiO_3/(R^{2+}TiO_3 + R_2O_3)$ alternatively expressed as $Mg/(R^{2+} + [R^{3+}/2])$.

[16] For the Lac Ellen sample AL7b, the most hematite-rich areas give compositions Ilm 24–25, Geik 1–2 (geikielite), and the most ilmenite-rich areas give Ilm 89–94.5, Geik 12.5–13.8. For Lac Tio sample AL23b the most hematite-rich areas give compositions Ilm 26–29, Geik 2–3, and the most ilmenite-rich areas give Ilm 90–91.5, Geik 13–13.8.

[17] EMP results for 257 points for sample AL36b are plotted in Figure 4a. The vertical axis of the Figure 4 is $2Ti/(2Ti + R^{3+})$, which is the equivalent of the fraction of $R^{2+}TiO_3$ "ilmenite" component to total $R^{2+}TiO_3 + R^{3+}_2O_3$. The horizontal axis $Mg/(R^{2+} + [R^{3+}/2])$ illustrates the fraction of $MgTiO_3$ (geikielite) substitution. These EMP analyses were performed in a series of stepped traverses designed to sample all parts of the grains from coarse hematite with abundant fine ilmenite exsolution to coarse ilmenite with abundant fine hematite exsolution, and also those marginal parts of coarse grains of both phases that
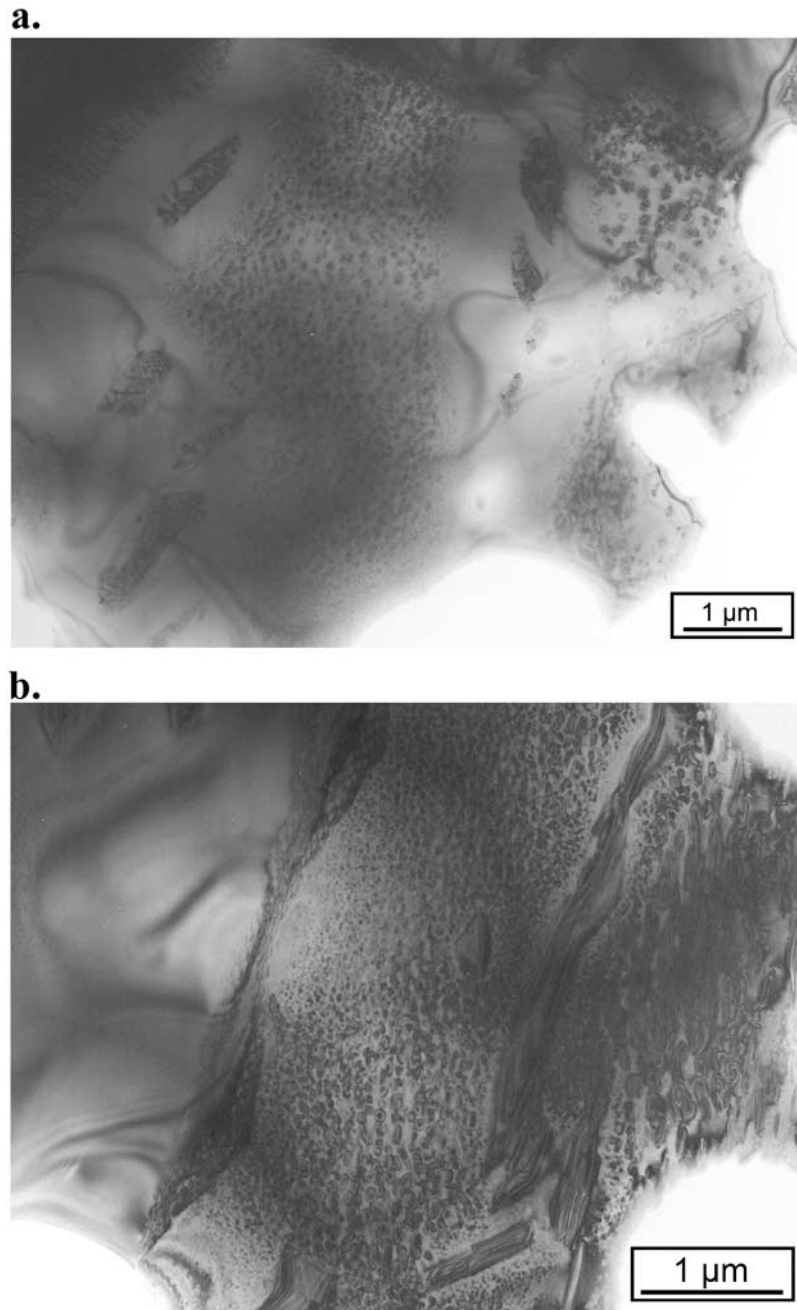
a.

b.

Figure 3. Bright field TEM images illustrating the different scales of exsolution in natural AL36b hemo-ilmenite. The images show a stranded microstructure with various generations of exsolution. (a) Ilmenite host with tiny (<20 nm) and medium-sized (0.5 μm) hematite exsolutions. Host ilmenite and hematite are in epitactic orientation relationship, whereby the **a** and **c** axes of both are parallel to each other. The tiny nanometer-sized hematite lenses are present in ilmenite regions, where larger hematite exsolutions are relatively widely spaced. As is typical for a stranded microstructure, these tiny hematite exsolutions are always absent in ilmenite regions adjacent to large hematite exsolutions (A and B). However, in regions where no discrete lamellae are visible, the hematite has developed a very fine scale mottling, indicative of chemical heterogeneity on a unit cell length scale. (b) A large hematite exsolution lamella (to right) more than 5 μm wide in an ilmenite host. These, as well as medium-sized exsolutions, contain numerous misfit dislocations at the interface to the surrounding host phase. The smallest and hence latest exsolutions are tiny ilmenite lenses within hematite a few nanometers thick. All tiny exsolutions are fully coherent with the surrounding host lattice and hence are not decorated with misfit dislocations. However, they are surrounded by shadows of strain contrast.

Table 2. Representative EMP Analyses of Ilmenite and Hematite From Sample AL36b With Structural Formulae, Calculated End-Members, and Plotting Ratios

	Extreme Ilmenite		Ilmenite Cluster		Extreme Hematite		Hematite Cluster	
	138a	133a	16i	143a	88i	83a	87i	48a
SiO_2, wt %	0.012	0.012	0.000	0.032	0.023	0.001	0.035	0.028
TiO_2	53.400	53.320	51.360	51.680	9.540	9.500	10.720	10.710
Al_2O_3	0.005	0.010	0.007	0.023	0.166	0.159	0.164	0.149
Cr_2O_3	0.048	0.012	0.034	0.039	0.423	0.342	0.414	0.368
V_2O_3	0.233	0.238	0.401	0.347	0.610	0.680	0.474	0.544
Fe_2O_3[a]	2.062	1.958	5.067	4.835	80.209	80.704	78.633	79.077
MgO	3.859	3.749	3.770	3.624	0.263	0.226	0.391	0.270
NiO	0.040	0.000	0.004	0.024	0.000	0.000	0.026	0.014
FeO[a]	40.834	41.048	39.251	39.859	8.137	8.142	8.935	9.116
MnO	0.278	0.228	0.167	0.128	0.000	0.000	0.000	0.045
ZnO	0.000	0.000	0.046	0.044	0.000	0.000	0.028	0.009
CaO	0.000	0.000	0.000	0.000	0.000	0.000	0.000	0.000
Total	100.772	100.575	100.107	100.635	99.371	99.753	99.820	100.330
FeO[b]	42.690	42.810	43.810	44.210	80.310	80.760	79.690	80.270
Total[b]	100.565	100.379	99.599	100.151	91.335	91.668	91.942	92.407
			Cations per Three O Atoms					
Si	0.0003	0.0003	0.0000	0.0008	0.0006	0.0000	0.0009	0.0007
Ti	0.9780	0.9791	0.9488	0.9506	0.1894	0.1879	0.2114	0.2104
Al	0.0001	0.0003	0.0002	0.0007	0.0052	0.0049	0.0051	0.0046
Cr	0.0009	0.0002	0.0007	0.0008	0.0088	0.0071	0.0086	0.0076
V	0.0045	0.0047	0.0079	0.0068	0.0129	0.0143	0.0100	0.0114
Fe^{3+}	0.0378	0.0360	0.0937	0.0890	1.5932	1.5977	1.5517	1.5542
Mg	0.1401	0.1364	0.1380	0.1321	0.0103	0.0088	0.0153	0.0105
Ni	0.0008	0.0000	0.0001	0.0005	0.0000	0.0000	0.0005	0.0003
Fe^{2+}	0.8317	0.8383	0.8064	0.8153	0.1796	0.1791	0.1960	0.1991
Mn	0.0057	0.0047	0.0035	0.0027	0.0000	0.0000	0.0000	0.0010
Zn		0.0000	0.0000	0.0008	0.0008	0.0000	0.0000	0.0005
Total	2.0000	2.0000	2.0000	2.0000	2.0000	2.0000	2.0000	2.0000
			Calculated Percentages of End-Members					
$FeSiO_3$	0.029	0.029	0.000	0.078	0.061	0.003	0.092	0.073
$MgTiO_3$	14.009	13.645	13.804	13.212	1.035	0.884	1.528	1.052
$NiTiO_3$	0.078	0.000	0.008	0.047	0.000	0.000	0.055	0.029
$FeTiO_3$	83.139	83.796	80.636	81.456	17.902	17.910	19.503	19.838
$MnTiO_3$	0.573	0.472	0.347	0.265	0.000	0.000	0.000	0.100
$ZnTiO_3$	0.000	0.000	0.083	0.079	0.000	0.000	0.054	0.017
Sum	97.829	97.942	94.879	95.139	18.997	18.797	21.232	21.109
Fe_2O_3	1.890	1.799	4.683	4.450	79.658	79.884	77.587	77.712
Cr_2O_3	0.046	0.012	0.033	0.038	0.441	0.356	0.429	0.380
V_2O_3	0.227	0.233	0.395	0.340	0.645	0.717	0.498	0.570
Al_2O_3	0.007	0.014	0.010	0.033	0.258	0.246	0.253	0.229
Sum	2.171	2.058	5.121	4.861	81.003	81.203	78.768	78.891
Total	100.000	100.000	100.000	100.000	100.000	100.000	100.000	100.000
			Plotting Ratios					
2Ti[c]	0.9783	0.9794	0.9488	0.9514	0.1895	0.1879	0.2116	0.2105
Cr[c]	0.0005	0.0001	0.0003	0.0004	0.0044	0.0036	0.0043	0.0038
V[c]	0.0023	0.0023	0.0039	0.0034	0.0065	0.0072	0.0050	0.0057
Al[c]	0.0001	0.0001	0.0001	0.0003	0.0026	0.0025	0.0025	0.0023
Mg/R^{2+}	0.1432	0.1393	0.1455	0.1389	0.0545	0.0470	0.0720	0.0498
Mg[d]	0.1401	0.1364	0.1380	0.1321	0.0103	0.0088	0.0153	0.0105

[a]Fe_2O_3 and FeO back-calculated after determining stoichiometric formula.
[b]Total Fe as FeO as in original EMP analysis and original sum.
[c]$2Ti + R^{3+}$.
[d]$R^{2+} + (R^{3+}/2)$.

were partially or completely freed of fine exsolution by marginal diffusion. It can be seen in Figure 4a that there are a few extreme analyses representing the most cleared out lamellar margins, and then major clusters of analyses that represent predominantly ilmenite and hematite host areas, but with abundant content of lamellae. Representative extreme and cluster analyses for ilmenite and hematite areas in sample AL36b are reported in Table 2. The highest ilmenite content analyses average ilmenite 97.9 and geikielite 13.9. The most hematite-rich areas average ilmenite 19.0 and geikielite 0.9. Although sample AL7b and AL23b EMP results are neither reported nor plotted here, the analyses lie on a virtually identical line to those in Figure 4a with respect to $MgTiO_3$ substitution.

[18] TEM-EDX analyses were performed at Bayerisches Geoinstitut, University of Bayreuth and evaluated according

to *Langenhorst et al.* [1995] and *McEnroe et al.* [2002]. These analyses were made mainly on host areas of ilmenite and of hematite most completely clear of fine exsolution. The advantage of the TEM-EDX analyses is that the small spot size and interaction volume allow analyses to be obtained of host areas between very fine lamellae, though the analytical precision is less than with the EMP method. However, even this technique is incapable of resolving proper analyses of a few nanometer-sized lamellae because the TEM foil is commonly thicker and exsolutions are lens shaped. For sample AL36b, there were nine acceptable analyses of ilmenite and nine also of hematite. The range of accepted ilmenite analyses was Ilm 95.1–100.3, Geik

12.8–14.3 with a mean of 97.6, 13.6. The range of accepted hematite analyses was Ilm 12.8–15.7, Geik 0.7–2.9 with a mean of 14.4, 1.8. Two typical examples of each are given in Table 3. For sample AL23b there were 5 acceptable analyses of ilmenite and 10 of hematite. The range of ilmenite analyses was Ilm 97.8–101.0, Geik 12.9–14.0, with a mean of 99.1, 13.4. The range of hematite analyses was Ilm 15.2–19.7, Geik 0.2–1.6 with a mean of 18.4, 0.7. Two typical examples of each are given in Table 3, but none are plotted in Figure 4.

[19]   Figure 4a illustrates the entire range of EMP analyses and the very strong fractionation of Mg into ilmenite and
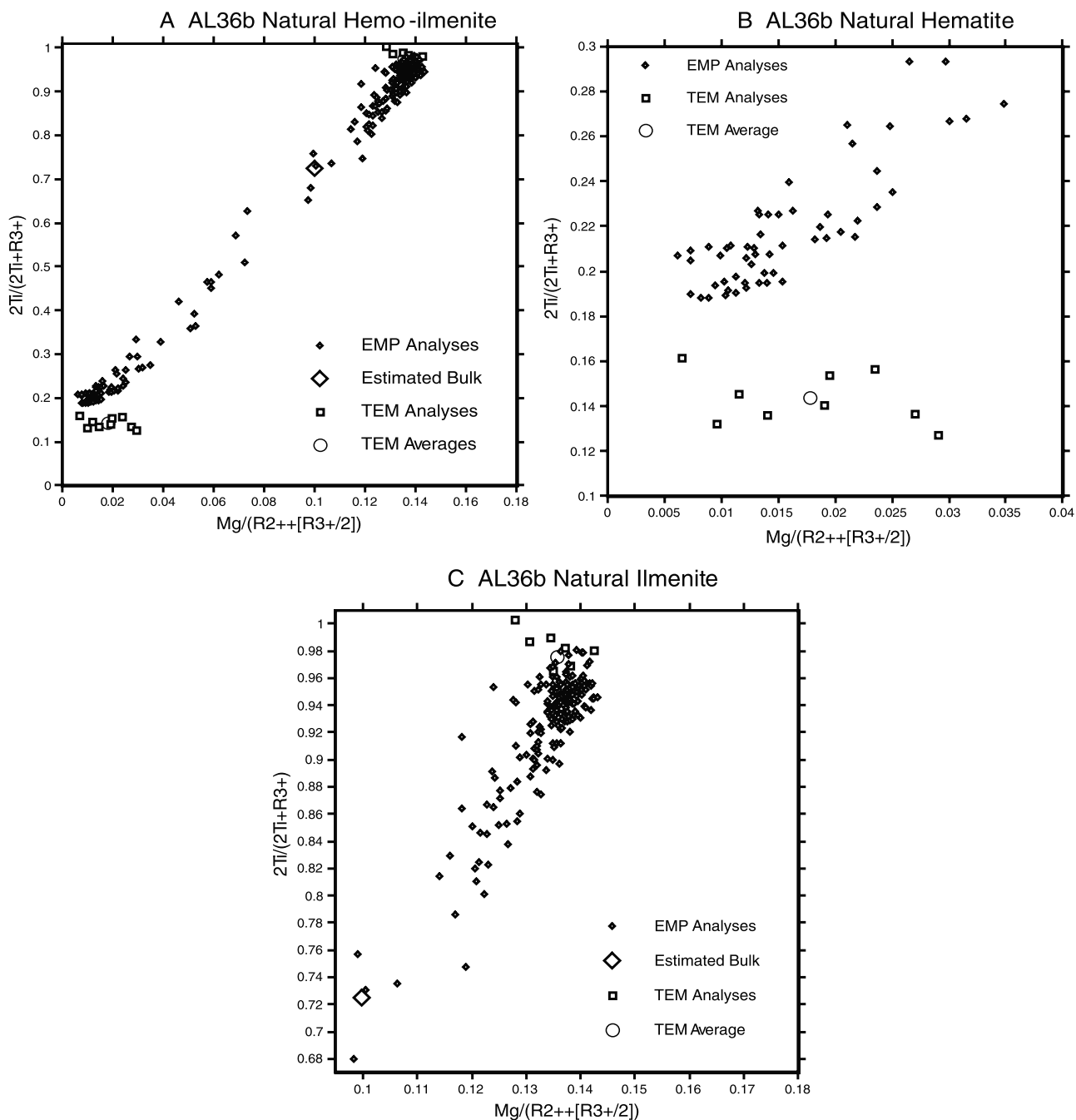

Figure 4

out of the ilmenite component of hematite. Similarly Cr and V are strongly fractionated into hematite. The broadening of the central trail of analyses between the two ends is caused by the effect on Mg analyses of mineral overlap on contacts between the two minerals. The bulk composition is based on a point-counted mode (3653 points) of a low-resolution backscatter image (hematite 29.5%, ilmenite 70.4%, spinel 0.08%) combined with averages of concentrations of analyses at the ilmenite and hematite ends (see Figures 4b and 4c). Expressed as ilm, geik, and hem, where ilm + geik + hem = 100, these are ilm 80.8, geik 13.7, hem 5.5 and ilm 18.9, geik 1.1, hem 80.0, yielding ilm 62.5, geik 10, hem 27.5.

[20] Figure 4b shows analyses in the hematite-rich part of the plot with exaggerated scale. There is a concentration of EMP analyses at the lower end, indicating grains dominated by hematite, in which the amount of fine ilmenite exsolution is minimal. These low-ilmenite-content analyses are ~ ilmenite 19.0 and geikielite 0.9. The TEM hematite analyses show a considerably lower content of ilmenite 12.8−15.7, average 14.4. The analytical results show that the EMP data represent hematite lamellae with small ilmenite exsolution lamellae; however, the TEM analyses at 14 probably give the true hematite compositions between the fine ilmenite lamellae.

[21] Figure 4c shows a close-up view of analyses in the ilmenite-rich part of the plot. There is a concentration of EMP analyses at the upper end, indicating grains dominated by ilmenite in which the amount of fine hematite exsolution is minimal. Aside from the tight grouping near the top, there are a few analyses from clearer areas next to coarse hematite lamellae. The highest ilmenite content analyses average ilmenite 97.9 and geikielite 13.9. The accepted TEM ilmenite analyses with an average ilmenite 97.6, geikielite 13.6 are consistent with this, despite a wider analytical scatter that can be attributed to the difficulty of subtracting the background of the continuum radiation [see *McEnroe et al.*, 2002].

5. Oxide Lattice Parameters by X-Ray Powder Diffraction

5.1. Analytical Methods

[22] A piece of AL36b was ground in an agate mortar, mixed with Si (NBS standard material 640) as an internal standard and characterized by means of X-ray powder diffraction at room temperature using a Philips X'Pert Pro X-ray diffraction system operating in reflection mode, equipped with Co-Kα_1 (λ = 1.78897Å) radiation selected with a focusing monochromator (a symmetrically cut curved Johansson Ge$_{(111)}$ crystal) and a Philips X'celerator detector. The diffraction pattern was collected in the 2θ range between 20° and 110° with step size 0.03°, and a scan speed of 0.004°/s and refined using a full pattern profile fitting (Rietveld analysis) with the program GSAS [*Larson and von Dreele*, 1994] and the Windows interface, EXPGUI

Figure 4. Electron microprobe (EMP) and TEM-EDX analyses on Allard Lake AL36b hemo-ilmenite. The vertical axis 2Ti/(2Ti + R^{3+}) is the equivalent of the fraction of R^{2+}TiO$_3$ "ilmenite" component (mostly FeTiO$_3$) versus Fe$_2$O$_3$ component, and the horizontal axis Mg/(R^{2+}+[R^{3+}/2]) illustrates the fraction of MgTiO$_3$ substitution, greatly exaggerated. The EMP analyses were performed in a series of stepped traverses designed to sample all parts of the grains from coarse hematite with abundant fine ilmenite exsolution to coarse ilmenite with abundant fine hematite exsolution, and also those marginal parts of coarse grains of both phases that had been most successfully cleared of fine exsolution by marginal diffusion. The TEM analyses were performed on what appeared to be host areas of ilmenite and of hematite most completely clear of fine exsolution. (a) Entire range of EMP analyses. Illustrates the very strong fractionation of Mg into ilmenite and out of the ilmenite component of hematite. Similarly (though not shown), Cr and V are strongly fractionated into hematite. The broadening of the central trail of analyses between the two ends is caused by the effect on Mg analyses of mineral overlap on contacts between the two minerals. The analyses were actually run in two sessions not shown separately. In the second session special effort was made to analyze "cleared out" areas on grain margins, and this session yielded the compositions closest to ilmenite and hematite end-members. The bulk composition is based on a point-counted mode (3653 points) of a low-resolution backscatter image (hematite 29.54%, ilmenite 70.38%, spinel 0.08%) combined with averages of concentrations of analyses at the ilmenite and hematite ends (Ilm 80.8, Geik 13.7, Hem 5.5; Ilm 18.9, Geik 1.1, Hem 80.0, see Figures 4b and 4c) yielding Ilm 62.53, Geik 9.97, Hem 27.50. (b) Close-up view of analyses in the hematite-rich part of the plot with exaggerated scale. There is a concentration of EMP analyses at the lower end, indicating grains dominated by hematite, in which the amount of fine ilmenite exsolution is minimal. These low ilmenite content analyses are about ilmenite 0.19 and geikielite 0.009. The TEM hematite analyses are much more scattered, even when certain widely scattered results are deleted. They do show a considerably lower content of ilmenite averaging 0.144. The higher geikielite at 0.18 cannot be explained by any likely chemical fractionating and seems certainly an analytical problem. The obvious conclusion from these analytical results is that all areas accessible to the electron probe beam, including the composition ilmenite 0.19, contain small ilmenite exsolution lamellae, but the TEM analyses at 0.144 probably give the true hematite compositions between the fine ilmenite lamellae. (c) Close-up view of analyses in the ilmenite-rich part of the plot with exaggerated scale. There is a concentration of EMP analyses at the upper end, indicating grains dominated by ilmenite in which the amount of fine hematite exsolution is minimal. Aside from the very tight grouping near the top, there are a few analyses from clearer areas next to coarse hematite lamellae. The five highest ilmenite content analyses average ilmenite 0.979 and geikielite 0.139. The TEM ilmenite analyses are reasonably consistent, when widely scattered results outside the limits Ilm 0.95−1.01 and geikielite 0.11−0.145 are deleted and yield an average Ilm 0.976, Geik 0.136. Because of scatter, the TEM average perhaps cannot be used to argue that there are no fine hematite lamellae within the most ilmenite-rich areas reached with the electron probe, though this is a possible conclusion.

Table 3. Representative TEM-EDX Analyses of Ilmenite and Hematite in Samples AL36b and AL23 With Structural Formulae, Calculated End-Members and Plotting Ratios

	Ilmenite AL36b		Hematite AL36b		Ilmenite AL23b		Hematite AL23b	
	03−2	03−7	17−4	17−23	03−2	03−7	17−4	17−23
O, at.%	60.00	60.00	60.00	60.00	60.00	60.00	60.00	60.00
Ti	19.65	19.61	2.94	2.91	19.85	19.55	3.51	3.77
Al			0.00	0.10				
Cr			0.17	0.19	0.02	0.02	0.07	0.07
Mg	2.74	2.85	0.67	0.23	2.61	2.73	0.16	0.19
Fe	17.52	17.45	36.50	36.57	17.41	17.62	36.25	35.97
Mn	0.07	0.08	0.00	0.00	0.10	0.07	0.00	0.00
Total	99.99	99.99	99.99	100.00	99.99	99.99	99.99	100.00
			Cations per Three O Atoms					
Ti	0.9825	0.9805	0.1470	0.1455	0.9925	0.9775	0.1755	0.1885
Al			0.0000	0.0050				
Cr			0.0085	0.0095	0.0010	0.0010	0.0035	0.0035
Fe^{3+}	0.0345	0.0385	1.6970	1.6945	0.0135	0.0435	1.6450	1.6195
Mg	0.1370	0.1425	0.0190	0.0115	0.1305	0.1365	0.0080	0.0095
$[Fe^{Tot}]$	[0.8760]	[0..8725]	[1.8250]	[1.8285]	[0.8705]	[0.8810]	[1.8125]	[1.7985]
Fe^{2+}	0.8415	0.8340	0.1280	0.1340	0.8570	0.8375	0.1675	0.1790
Mn	0.0040	0.0040	0.0000	0.0000	0.0050	0.0035	0.0000	0.0000
Total	1.9995	1.9995	1.9995	2.0000	1.9995	1.9995	1.9995	2.0000
			Calculated Percentages of End-Members					
$MgTiO_3$	13.70	14.25	1.90	1.15	13.05	13.65	0.80	0.95
$FeTiO_3$	84.15	83.40	12.80	13.40	85.70	83.75	16.75	17.90
$MnTiO_3$	0.40	0.40	0.00	0.00	0.50	0.35	0.00	0.00
Sum	98.25	98.05	14.70	14.55	99.25	97.75	17.55	18.85
Fe_2O_3	1.73	1.93	84.85	84.73	0.68	2.18	82.25	80.98
Cr_2O_3			0.43	0.48	0.05	0.05	0.18	0.18
Al_2O_3			0.00	0.25				
Sum	1.73	1.93	85.28	85.45	0.73	2.23	82.43	81.15
Total	99.98	99.98	99.98	100.00	99.98	99.98	99.98	100.00
			Plotting Ratios, Summations					
2Ti[a]	0.9827	0.9807	0.1470	0.1455	0.9928	0.9777	0.1755	0.1885
Cr[a]			0.0043	0.0048	0.0005	0.0005	0.0018	0.0018
Al[a]			0.0000	0.0025				
Mg/R^{2+}	0.1394	0.1453	0.1293	0.0790	0.1315	0.1396	0.0456	0.0504
Mg[b]	0.1370	0.1425	0.0190	0.1150	0.1305	0.1365	0.0080	0.0095
a	1.9995	1.9995	1.9995	2.0000	1.9995	1.9995	1.9995	2.0000
b	0.9998	0.9998	0.9998	1.0000	0.9998	0.9998	0.9998	1.0000
R^{4+}	0.9825	0.9805	0.1470	0.1455	0.9925	0.9775	0.1755	0.1885
R^{3+}	0.0345	0.0385	1.7055	1.0709	0.0145	0.0445	1.6485	1.6235
R^{2+}	0.9825	0.9805	0.1470	0.1455	0.9925	0.9775	0.1755	0.1885

[a]$2Ti + R^{3+}$.
[b]$R^{2+} + (R^{3+}/2)$.

[*Toby*, 2001]. Three phases (apart from the Si standard) were found to be present in the diffraction pattern: ilmenite, hematite and spinel. The zero position of the diffraction pattern was refined based on the Si standard peak positions (a = 5.43088), background function, scale factors, unit cell parameters of the three phases present, and broadening coefficients of the pseudo-Voigt profile function also were refined.

5.2. Results and Interpretation

[23] Refinement of the X-ray powder diffraction pattern yielded the following lattice parameters in Å: Dominant ilmenite-rich composition: a = 5.0828(2), c = 14.0498(6), unit cell volume = 314.34(1) Å³. Subordinate hematite-rich composition: a = 5.0441(2), c = 13.7702(9), unit cell volume = 303.42(2) Å³. The diffraction peaks of both phases are relatively sharp, indicating that compositions range over a very few percent. The pattern indicated the presence of an Mg-spinel with parameters (a = 8.1194(2) Å) slightly larger than pure $MgAl_2O_4$.

[24] A compositional interpretation from the unit cell volumes is made in the context of the ternary system Fe_2O_3-$FeTiO_3$-$MgTiO_3$. For Fe_2O_3-$FeTiO_3$ we used a compilation of *Harrison* [2006] which includes the compositions studied by *Brown et al.* [1993] plus compositions Ilm 70, 80, 90 synthesized by Harrison with unit cell volumes determined by neutron diffraction. A notable and long-recognized feature of this series is the negative volume of mixing that was not taken into account in studies before 1965. For the join $FeTiO_3$-$MgTiO_3$, we used end-member ilmenite from the Harrison plot plus the cell volume of $MgTiO_3$ [*Waychunas*, 1991] at 307.558 Å³, and assumed a linear relationship.

[25] For the ilmenite composition, we used the EMP analyses of ilmenite to project the composition to a pure ilmenite end-member at $Mg/(Mg + Fe^{2+}) = 0.142$, which

indicates a cell volume of 314.64 $\mathring{A}^3$. We then constructed an approximate cell volume profile along the joint Fe_2O_3-$Mg_{0.142} Fe^{2+}_{0.858}TiO_3$, based mainly on the Fe_2O_3-$FeTiO_3$ profile, and used 314.34 $\mathring{A}^3$ to estimate an Ilm content of 97.17–98.16.

[26] For the hematite composition the EMP analyses of hematite were used to project the composition of the ilmenite component to a pure ilmenite end-member at $Mg/(Mg + Fe^{2+}) = 0.047$, which indicates a cell volume of 315.43 $\mathring{A}^3$. A cell volume profile along the join from this to hematite gives only a very slight volume difference from the Fe_2O_3-$FeTiO_3$ join, because the hematite is very close to it in composition. Here the cell volume 303.42 $\mathring{A}^3$ indicates a composition Ilm 12.13–12.58.

[27] Considering the different methods and uncertainties, the general consistency is very good. For the ilmenite composition, where we have valid EMP analyses for areas cleared of fine hematite exsolution, the average is 97.9 compared to the lattice parameter estimate of 97.7–98.16. This compares to TEM-EDX analyses with a range 95.1–100.3. For the hematite composition, there are no areas free of fine ilmenite lamellae that could be analyzed by EMP, so comparison can only be made with the TEM-EDX analyses with a range 12.8–15.7 and average 14.4, compared to the lattice parameter estimate of 12.13–12.58.

[28] The nature of phase relations in the hematite-ilmenite system might suggest that there are multiple opportunities to trap a variety of metastable phase compositions during exsolution. Textural evidence in Figure 3 demonstrates that such trapped gradients were established during high-T exsolution in the $R\bar{3}c$ hematite + $R\bar{3}$ ilmenite region, and this concept was used to explain chemical and magnetic evolution. Yet the available chemical and lattice parameter data suggest there was likely chemical convergence during the coolest and most long-lived exsolution in the CAF $R\bar{3}c$ hematite + $R\bar{3}$ ilmenite field. Evidence for similar convergence is also available in exsolved pyroxenes [*Robinson*, 1980], which commonly preserve limited composition ranges even though physical patterns of exsolution have left a record of long-lived evolution and chemical change. This is a subject for future research at and beyond the spatial limits of present analytical methods.

6. Origin of Remanence and Coercivity and Keys to Magnetic Structure

[29] Here we present theoretical background and phase diagram interpretation anticipating the detailed interpretation of the specific Mössbauer and magnetic results to follow.

6.1. Lamellar Magnetism Hypothesis

[30] Recent detailed studies on chemistry, crystal structure and magnetic properties of highly exsolved rhombohedral oxides, both ilmenite with hematite lamellae (hemo-ilmenite) and hematite with ilmenite lamellae (ilmeno-hematite) showed that the high NRM and coercivity values were not explained by the properties of either AF hematite nor PM ilmenite alone [*McEnroe and Brown*, 2000; *McEnroe et al.*, 2001a, 2001b, 2002, 2004a, 2004b, 2004c, 2005; *Kasama et al.*, 2004]. Because the properties seemed to occur in many different bulk compo-

sitions, but all having the characteristic of fine exsolution, it seemed likely that the properties were linked to the intergrowths themselves. Explorations of magnetic properties of lamellar interfaces, including Monte Carlo simulations of lamellar formation involving atomic and magnetic interactions between Fe^{2+}, Fe^{3+} and Ti^{4+} ions demonstrated the magnetic significance of these interfaces, and from these studies the hypothesis of "lamellar magnetism" developed [*Harrison and Becker*, 2001; *Robinson et al.*, 2002, 2004, 2006]. Later studies of the orientations of magnetic moments in hemo-ilmenite single crystals [*Robinson et al.*, 2006] have shown these orientations to be compatible with details of the hypothesis.

[31] Essential aspects of the hypothesis are illustrated in Figure 5. This shows the magnetic moments of hematite Fe^{3+} layers, and mixed Fe^{2+} and Fe^{3+} contact layers parallel to the (0001) basal plane related to an ilmenite lamella 2 unit cells thick. The top and bottom hematite layers have opposite magnetic moments, so the entire model can be repeated to produce a larger volume of lamellar magnetic material. Within the hematite there is an ilmenite lamella consisting of 6 Ti layers and 5 Fe^{2+} layers. The Fe^{2+} from a 6th layer is incorporated with Fe^{3+} from hematite in the two contact layers. In this particular model there is a 50:50 ratio of canted antiferromagnetic hematite and paramagnetic ilmenite. Each of the two contact layers has a magnetic moment of $\sim$4.5 μB and is countered by the $\sim$5 μB magnetic moment of one unbalanced hematite Fe^{3+} layer, giving a total magnetic moment of 9 – 5 = $\sim$4 μB for one lamella (large arrow), and a total magnetic moment of 4/12 = $\sim$0.333 μB per formula unit.

[32] A key to having a strong lamellar magnetism is to develop a high yield of small lamellae and to have them magnetically in-phase. The development of lamellae that are magnetically in-phase depends on the orientation of the magnetizing field relative to the (0001) basal plane during nucleation and growth of the lamellae. Thus the magnetizing field is the so-called "external force" of lamellar magnetism, creating in-phase lamellae when the (0001) basal plane is parallel to the field, but incapable of doing so when the basal plane is perpendicular to the field. Higher coercivity, where the dominant host of fine lamellae is hematite, than where it is ilmenite, is well explained by details of the hypothesis. The phase diagram of the hematite-ilmenite system is also a key to development of magnetized lamellae.

6.2. Phase Diagram of the Hematite-Ilmenite System

[33] A revised 1-atm phase diagram for the hematite-ilmenite system [*Harrison*, 2006] is given in Figure 6 and is used to interpret mineral evolution. There are differences with earlier versions [*Harrison*, 2000; *Harrison and Becker*, 2001; *Robinson et al.*, 2004]. Positions of the magnetic- and cation-ordering phase transitions are known with some certainty, and are well constrained by experimental data [*Ishikawa and Akimoto*, 1957; *Ishikawa et al.*, 1985; *Harrison et al.*, 2000a; *Harrison and Redfern*, 2001]. The miscibility gap, however, is poorly constrained by experimental data and estimates of its position made using different thermodynamic approaches vary considerably [e.g., *Burton and Kikuchi*, 1984; *Burton*, 1984, 1985, 1991; *Ghiorso*, 1997; *Harrison et al.*, 2000b; *Harrison*
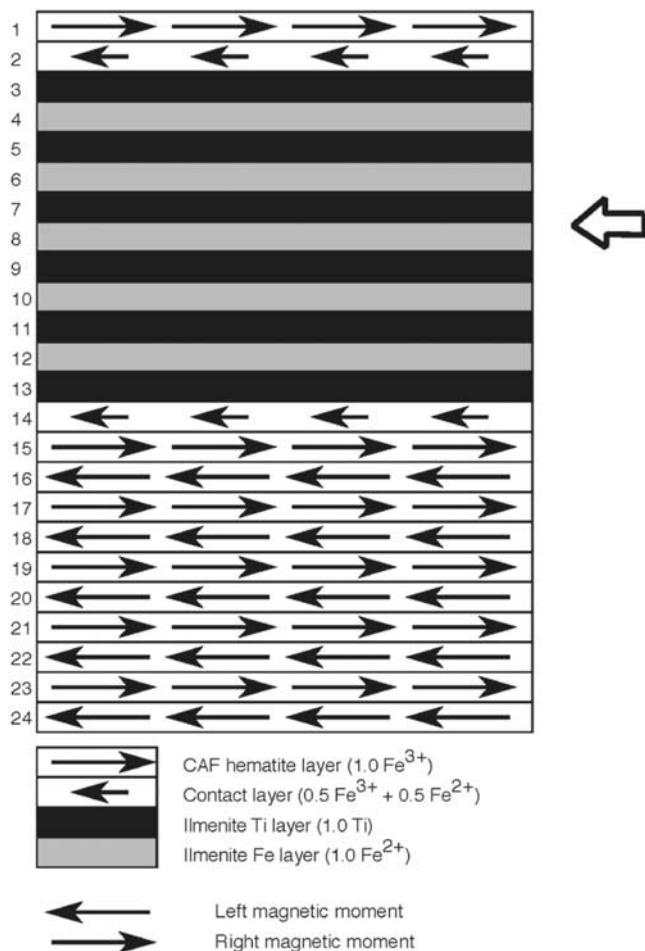
Figure 5. Schematic illustration of a 24-layer model of lamellar magnetism, showing the magnetic moments of hematite Fe^{3+} layers, and mixed Fe^{2+} and Fe^{3+} contact layers parallel to the (001) basal plane related to an ilmenite lamella 2 unit cells thick. The top and bottom hematite layers have opposite magnetic moments, so the entire model can be repeated to produce a larger volume of lamellar magnetic material. Within the hematite there is an ilmenite lamella consisting of 6 Ti layers and 5 Fe^{2+} layers. The Fe^{2+} from a sixth layer is incorporated with Fe^{3+} from hematite in the two contact layers. In this particular model, there is a 50:50 ratio of canted antiferromagnetic hematite and paramagnetic ilmenite. Each of the two contact layers has a magnetic moment of ~4.5 μB and is countered by the ~5 μB magnetic moment of one unbalanced hematite Fe^{3+} layer, giving a total magnetic moment of $9 - 5 = \sim 4$ μB for one lamella (large arrow), and a total magnetic moment of $4/12 = \sim 0.333$ μB per formula unit. A key to having a strong lamellar magnetism is to develop a high yield of small lamellae and to have them magnetically in-phase, which depends on the orientation of the magnetizing field relative to the (001) basal plane during nucleation and growth of the lamellae. Higher coercivity, where the dominant host of fine lamellae is hematite, than where it is ilmenite, is well explained by details of the hypothesis. The phase diagram of the hematite-ilmenite system is a key to development of magnetized lamellae.

and Becker, 2001]. All thermodynamic models predict the presence of a miscibility gap below $975-1075$ K, separating a paramagnetic hematite-rich phase (PM $R\bar{3}c$) from a paramagnetic ilmenite-rich phase (PM $R\bar{3}$). At lower T, the hematite-rich limb of the miscibility gap approaches the magnetic ordering transition, causing the PM $R\bar{3}c$ phase to become canted antiferromagnetic (CAF $R\bar{3}c$). Under equilibrium conditions, magnetic ordering in the hematite-rich phase leads to the eutectoid reaction PM $R\bar{3}c \rightarrow$ CAF $R\bar{3}c$ + PM $R\bar{3}$, and a pronounced widening of the miscibility gap. Estimates of the T of the eutectoid reaction vary between ~665 K [*Ghiorso*, 1997; *Harrison and Becker*, 2001; *Robinson et al.*, 2004] and 800 K [*Burton*, 1985; *Harrison*, 2006], while estimates of its position vary between 20 and 31 mol % ilmenite (Ilm $20-31$). The equilibrium state at low T consists of an intergrowth of CAF $R\bar{3}c$ and PM $R\bar{3}$ phases, with compositions that diverge toward pure hematite and pure ilmenite, respectively. The size distribution and spatial arrangement of these phases is a complex function of the cooling history.

6.3. Evolution of Allard Lake Exsolution and Magnetism

[34] The evolution of sample AL36b, considered typical, is qualitatively illustrated on Figure 6. The possible effects of pressure on the phase diagram under natural conditions are discussed elsewhere [*McEnroe et al.*, 2004a, 2004b, 2004c; *Harrison et al.*, 2006]. These effects would generally give higher exsolution/ordering T than mentioned here and more ilmenite-rich ilmenites. The interpretation is based on the approximate bulk composition of the hemo-ilmenite at Ilm 72.5 and on the TEM compositions of hematite host grains at Ilm 14.4 in regions containing fine ilmenite lamellae. The electron microprobe (EMP) analyses of hematite-rich compositions generally track the compositions of coarse hematite believed to have been $R\bar{3}c$ before the latest exsolution and come down to about Ilm 20. EMP and TEM analyses of ilmenite are consistently more Ti-rich than those illustrated on the phase diagram at moderate T. This is true of all natural compositions we have studied in Rogaland Norway, SW Sweden, Adirondacks, NY and Allard Lake [*McEnroe and Brown*, 2000; *McEnroe et al.*, 2001a, 2001b, 2002, 2004a, 2004b, 2004c, 2005; *Kasama et al.*, 2004] all probably exsolved at pressures of $5-10$ kbar, suggesting exploration of the pressure effects on the equilibria are needed. We do not attempt here to interpret compositions of ilmenite and its hematite exsolution, but suggest that the coarse hematite and its fine ilmenite exsolution are likely the more important carrier of remanence, as also indicated by Hargraves' chemical etch experiments [*Robinson et al.*, 2004].

[35] At high T, above 1000 K, the Allard Lake Ilm 72.5 mineral was a homogeneous $R\bar{3}$ ilmenite. It reached the solvus limb at 975 K (702°C) (path 1), and the initial equilibrium paramagnetic $R\bar{3}c$ hematite would have had composition Ilm 49.9. If cooled metastably without chemical change, such a hematite would have a magnetic ordering T of 500 K (227°C). If continuously equilibrated down to 800 K (path 2), it would then consist of 21.6% of $R\bar{3}c$ hematite Ilm 20 in 78.4% host of Ilm 87. At this T both phases would be paramagnetic.
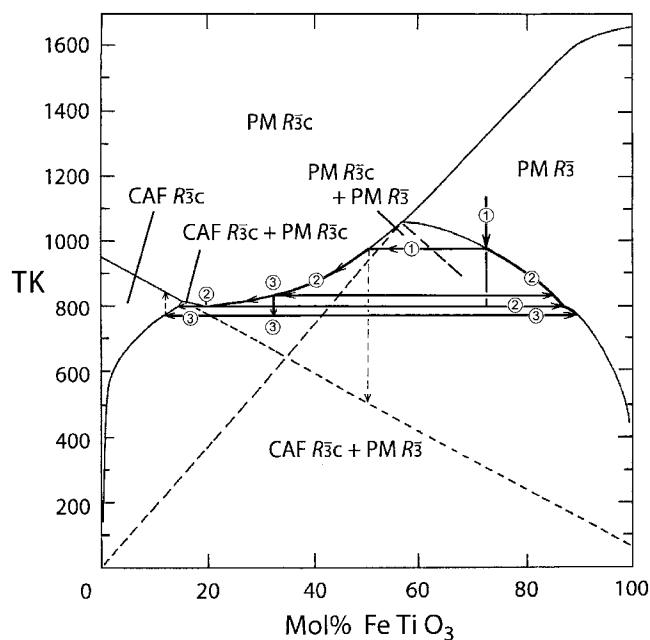
Figure 6. Revised 1-atm phase diagram for the hematite-ilmenite system [*Harrison*, 2006] above room T showing three single-phase regions: (1) cation-disordered paramagnetic $R\bar{3}c$ hematite, (2) cation-ordered paramagnetic $R\bar{3}$ ilmenite, and (3) cation-disordered, magnetically ordered canted-antiferromagnetic CAF $R\bar{3}c$ hematite. Oppositely oriented magnetic- and cation-ordering schemes extend to metastable regions, producing two "tricritical" points [*Burton*, 1985, 1991], and the eutectoid at ~800 K, where $R\bar{3}c \rightarrow$ CAF + $R\bar{3}$. CAF hematite coexists with ilmenite only below this T, the realm of lamellar magnetism. For X Ilm > eutectoid, magnetization is impossible for T > eutectoid. Magnetization develops during exsolution, below T Néel of hematite; thus remanent magnetization is chemical not thermal [*Robinson et al.*, 2002, 2004]. Three hypothetical stable and metastable cooling paths are indicated 1, 2, 3, describing evolution of Allard Lake hemo-ilmenite.

[36] If equilibrium cooling continued at 800 K (path 2), a three-phase reaction would take place converting $R\bar{3}c$ paramagnetic hematite with composition Ilm 20 to 92.3% CAF hematite of composition Ilm 14.4 (coincidentally TEM composition of AL36b) and 7.7% of $R\bar{3}$ ilmenite of composition Ilm 87 (path 2). This is the highest T where any magnetic material could be produced from bulk composition Ilm 72.5, and would provide an opportunity for development of lamellar magnetism. If equilibrated just below the eutectoid T, the original bulk composition would consist of 80% PM ilmenite and 20% CAF hematite. Assuming lack of chemical reequilibration the lamellar magnetism would be locked to the antiferromagnetism of the CAF hematite host, ignoring possible effects of lattice strain would have a T_N of 821 K (548°C). Here we use T_N and not T_C because, though lamellar magnetism is a ferrimagnetic substructure, in this case it is locked to the canted AF hematite.

[37] During the course of various stages of diffusional equilibration, trapped gradients would develop as shown in the TEM images (Figure 3). From these trapped gradients, various compositions of $R\bar{3}c$ hematite would undergo undercooling and bypass the equilibrium three-phase reaction (Figure 6). For example, using a $R\bar{3}c$ hematite composition trapped at 834 K (561°C) with composition Ilm 33.3 (path 3) and cooling metastably to 775 K (502°C) (path 3), a eutectoid reaction would produce 73.1% of CAF hematite Ilm 12.2 and 26.9% of $R\bar{3}$ ilmenite lamellae of composition Ilm 89.5 (path 3). This undercooling reaction provides a substantial yield for lamellar magnetism. The resulting abundant CAF hematite should have a strain-free T_N of 841 K (568°C), or 66° above its exsolution T. In sample AL36b, the hematite with TEM composition Ilm 14.4 has a T_N of 893 K (620°C), over 70°C above its predicted strain-free T_N of 821 K. This increase may be related to lattice strain along the many coherent lamellar contacts, and/or related to the nature of the contact layers.

[38] A key feature of this interpretation is that the magnetism of the Allard Lake samples is a chemical remanent magnetization (CRM), made possible by the chemical exsolution of CAF hematite from a paramagnetic host at a T according to the phase diagram below 800 K (527°C). It could not be a thermal remanent magnetization (TRM), because the CAF phase was already well below its Nèel T at the moment it was created by exsolution.

6.4. Low-T Phase Relations

[39] Figure 7 shows phase relations at 1 atm for the ilmenite-rich part of the system Fe_2O_3-$FeTiO_3$ from Ilm 60 to Ilm 100 in the T range 400–0 K. The phases with annealing T at 1573–973 K achieved nearly complete Fe^{2+}-Ti ordering at high T [*Harrison*, 2000; *Harrison and Redfern*, 2001], at least above Ilm 75, and all except compositions above ~Ilm 95 are metastable with respect to CAF $R\bar{3}c$ hematite + $R\bar{3}$ ilmenite below 800 K. The chemical ordering T, from ~1650 K to 1100 K, are well above any T causing exsolution, which is 1050 K for Ilm 60 and lower for more Ti-rich compositions. Two samples Ilm 61.8 and ilm 68.8 were annealed at 973 K below the peak of the solvus but showed no exsolution in experiments lasting over 3 years [*Burton*, 1982]. On the basis of the work by *Ishikawa et al.* [1985] and related neutron scattering studies [*Arai et al.*, 1985a; *Arai and Ishikawa*, 1985; *Arai et al.*, 1985b], and new data, a more structured arrangement of the boundaries was made (B. P. Burton et al., A low-T magnetic phase diagram for ilmenite-rich compositions in the system Fe_2O_3-$FeTiO_3$, submitted to *American Mineralogist*, 2007, hereinafter referred to as Burton et al., submitted manuscript, 2007). Here it is shown specifically for the geikielite-substituted Ilm 98 composition of sample AL36b, which reached its composition by exsolution at T perhaps as low as 650 K, thus avoiding most complexities of more Fe_2O_3-rich ilmenites.

[40] Two types of magnetic interactions are involved in phase properties. One is superexchange through oxygen of Fe atoms in adjacent octahedral layers, producing sublattice magnetizations parallel to the (0001) basal plane of the rhombohedral oxide, with opposite moments in adjacent layers. This is impossible in end-member ilmenite, where Fe atoms occur only in alternate layers. The other type is between Fe atoms in ordered layers separated by one layer of Ti and two layers of oxygen, as in end-member ilmenite.
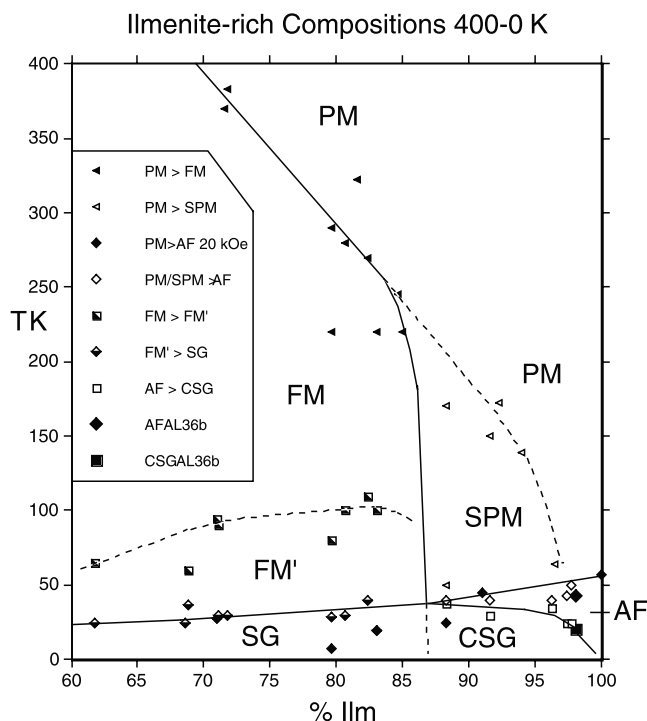
Ilmenite-rich Compositions 400-0 K

Figure 7. Preliminary low-T phase diagram for cation-ordered ferri-ilmenite compositions in the system Fe_2O_3-$FeTiO_3$ (adapted from Burton et al. (submitted manuscript, 2007)). Major fields of paramagnetism (PM), ferrimagnetism (FM), superparamagnetism (SPM), and antiferromagnetism (AF) are shown, as well as three different regions of spin-glass-like behavior (FM′, SG, and CSG) and illustrate the complex interplay of adjacent layer magnetic ordering as in hematite and double-layer magnetic ordering as in ilmenite.

This produces magnetization normal to the basal plane and parallel to the crystallographic **c** axis with opposite moments in the wider-spaced layers. The two types are incompatible, both in terms of antiferromagnetic relationships and magnetic moment orientation. This creates most of the phase structures involved.

[41] For compositions Ilm 60–86, superexchange between Fe in adjacent layers produces strong AF interactions, but alternate layers have more and less Fe ions, giving a ferrimagnetic (FM) structure, with strong moments parallel to (0001). The PM → FM transition declines as X Ilm rises, because the amount of Fe^{3+} in Ti-rich layers declines. When X Ilm > 85, Fe^{3+} in Ti layers is so low that FM ordering is unstable; but, local ferrimagnetic clusters form, yielding superparamagnetic-like (SPM) properties, and a PM→SPM crossover with continued fall in T. Below ∼100 K the magnetization of the FM phase declines sharply (FM′) due to increasing strength of misaligned frustrated moments at the edges of magnetized regions, leading toward reentrant spin glass behavior.

[42] A second major boundary separates the PM (or SPM) phase above from the antiferromagnetic (AF) ilmenite below, caused by onset of two-layer interactions, producing a perfect antiferromagnet with magnetic moments parallel to **c**. Dilution of $FeTiO_3$ with Fe^{3+} in Fe and Ti layers (and with Mg in Fe layers in AL36b) disrupts two-layer ordering, so the line PM (or SPM) → AF declines with declining X Ilm. Points for this transition in a strong magnetic field are shown by the black symbols, but they are at a higher T in a weaker field for composition Ilm 88 [*Ishikawa et al.*, 1985]. For compositions Ilm 83 to Ilm 62, there is a boundary FM′ → SG, but it is presently uncertain if this represents imposition of two-layer ordering on former FM with reentrant spin-glass-like behavior, or is a behavior produced only by single-layer ordering [*Ishikawa et al.*, 1985]. Below AF ordering T for compositions > Ilm 85, single-layer ordering similar to that producing the SPM-like clusters appears to come into increasing frustration with AF double-layer ordering, producing cluster spin glass (CSG) described for Ilm 88 by *Arai et al.* [1985a] and *Ishikawa et al.* [1985] and in new data for ilm 91.5 and 97.4 (Burton et al., submitted manuscript, 2007).

[43] The ilmenite host sample AL36b, with ∼Ilm 98 composition ($FeTiO_3$ 84, $MgTiO_3$ 13.9, Fe_2O_3 2.1) avoids most complications. It attains a peak of antiferromagnetic magnetization at 43 K, which then falls off to a sharp break at 20 K where this composition appears to behave as a cluster spin glass (CSG). However, for sample AL36b, there is another possibility, because of abundance of hematite-ilmenite interfaces, where hematite is already magnetized at high T. Thus the spin glass-like behavior in this sample at and below 20 K, could reflect conditions in which the two-layer magnetization of the ilmenite host starts to invade the strong adjacent layer interactions along hematite interfaces, so that multiple frustrations develop. Further investigation of this phenomenon is in progress, because of its importance to the concept of lamellar magnetism.

7. Mössbauer Spectroscopy

[44] Mössbauer spectra were obtained at Department of Physics, Technical University of Denmark, using constant acceleration spectrometers and a source of ^{57}Co in rhodium. The centroid of the spectra is given relative to that of α-Fe. Sample AL23d (companion to specimens to AL23b,c) was studied using room T and low-T Mössbauer spectroscopy, obtained with and without an applied magnetic field [*Frandsen et al.*, 2007a, 2007b]. Additionally, AL36b was recently measured at room T and low T. A key observation in AL36b and AL23d runs was that the spectra contained no indication of the presence of magnetite. This has been verified from the clear absence of the characteristic B site component in room T Mössbauer spectra of magnetite. At room T and down to ∼45 K the spectra of AL23d and AL36b are dominated by the six-line spectrum of Fe^{3+} in CAF titanohematite and a doublet characteristic of Fe^{2+} in paramagnetic ilmenite. In Figure 8, showing low-T Mössbauer spectra of AL36b, similar spectral behavior is observed for 60 K and 45 K. At 40 K and below, the doublet was replaced by a sextet from Fe^{2+}, indicating the presence of ilmenite below its T_N, i.e., that the T_N is between 40 and 45 K consistent with low-T susceptibility measurements discussed below. From spectral behavior of hematite, we find that the Morin transition is absent at all studied T. Though the hematite lamellae in ilmenite range in size from 40 microns down to a few nanometers, evidence for superparamagnetic
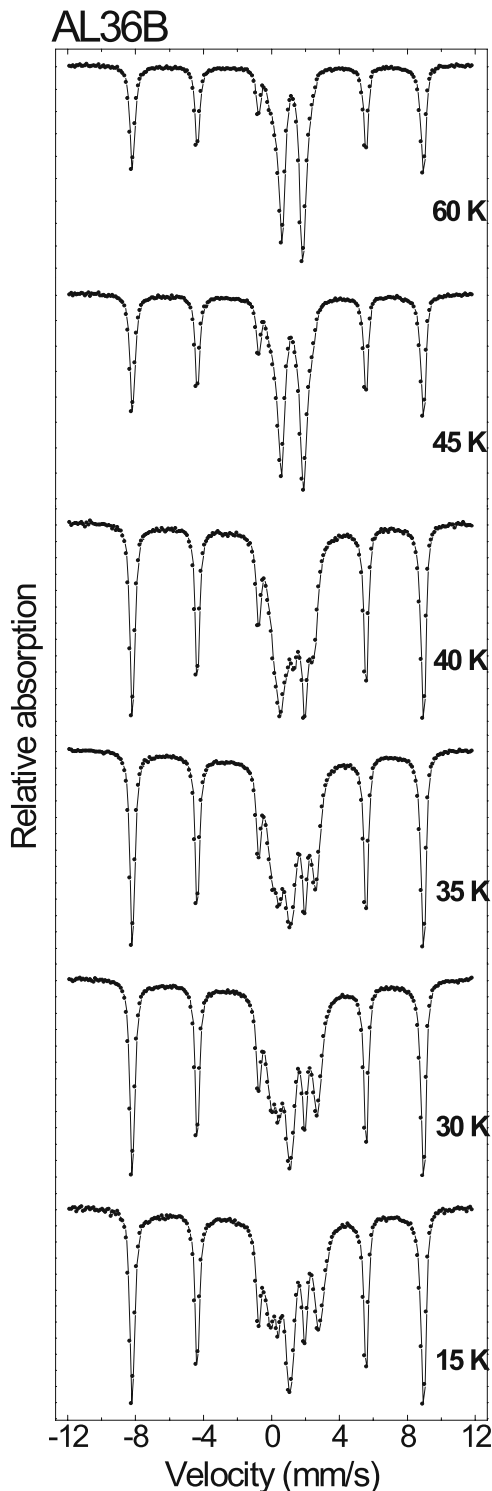
AL36B

Figure 8. Mössbauer spectra of AL36b obtained at 60, 45, 40, 35, 30, and 15 K. The velocities of the spectra are given relative to the centroid of the calibration spectra of α-Fe. As an aid to the eye, solid lines connect data points. The spectra show magnetically ordered hematite at all T, and ilmenite ordering with a T_N between 45 and 40 K.

behavior of the small hematite lamellae was not observed in the spectra at any temperature.

8. Rock Magnetic Properties

8.1. Laboratory Techniques

[45] Magnetic experiments were made at the Geological Survey of Norway (NGU), the Institute for Rock Magnetism (IRM), University of Minnesota, and the Paleomagnetic Lab at CSIRO, Australia. The NRM intensities of Allard Lake ores are too great for measurement on a cryogenic magnetometer. Remanent magnetization was measured using a fluxgate spinner magnetometer (DIGICO) at CSIRO, or on a JR6 magnetometer at NGU. Bulk susceptibility (k) was measured using a transformer bridge with sensitivity of 10^{-6} SI at CSIRO, or at the NGU Petrophysics Laboratory. Hysteresis measurements were made in fields up to 1.5 T on a Princeton vibrating sample magnetometer (VSM) at IRM or NGU. Low-T remanence measurements were made on a Quantum Design (MPMS2) Squid magnetometer at IRM. Temperature and frequency dependence of susceptibility were measured with the MPMS2 at frequencies between 0.1 Hz and 1 kHz, in the T range of $5-300$ K, in fields of 279 A/m.

8.2. Susceptibility, NRM, and Demagnetization Behavior

[46] Our measured susceptibilities of the Lac Tio and Lac Ellen samples ranged from 5.1 to 114 $\times$ 10^{-3} SI (Table 4). High-susceptibility samples contain magnetite; low-susceptibility samples contain only hemo-ilmenite. NRM values range from 32 to 120 A m^{-1}, with an average of 63 A m^{-1}. These measurements are consistent with measurements made by R. B. Hargraves in the 1980s (see Table 1); however, the NRMs are higher than NRMs reported by *Hargraves* [1959a], which are off by about one decimal place (R. B. Hargraves, personal communication, 2003). The samples studied here all have high Koenigsberger ratios, Q = NRM/kH, from 9 to 543, calculated for the local field value of 52,102 nT.

[47] To evaluate the contribution of soft components, low-T demagnetization experiments (see Figure 1) were made in a field-free (FF) environment by cooling three samples in dry ice (193 K) at a temperature below the Morin transition for hematite (263 K) but above the Verwey transition (120 K) for magnetite. Samples showed no loss in magnetization. Samples were then cooled in a bath of liquid nitrogen (77 K) and warmed back to room T in field-free conditions. The high susceptibility samples AL20c, and AL114b both containing magnetite, showed a 22% and 6% increase in NRM intensity, respectively, whereas the lowest-susceptibility sample AL36b showed a 2% loss in NRM upon warming back to room T. The dominant NRM in the ores is reversed and the magnetite likely carries a normal overprint. Sample AL114b was then AF demagnetized up to 90 mT with no further loss in NRM (see Figure 1). The high resistance to AF demagnetization is typical for Allard Lake samples that lack, or contain, only a small amount of magnetite. Thermal unblocking of low susceptibility samples is between 600 and 620°C with tails persisting to 630°C (see Figure 1). The higher susceptibility samples

Table 4. Rock Magnetic Measurements on Lac Tio and Lac Ellen Samples From the Present Study

Sample	NRM, A/m	Density, kg/m^3	Susceptibility, SI 10^{-6}	Q
7b[a]	120	4629	0.005343	543
20c	43	4705	0.113355[b]	9
23b	77	4532	0.006585	281
36b	32	4679	0.005057	150
46b	73[b]	4691	0.065747	27
114b	34	4604	0.024479	33

[a]Sample 7b from Lac Ellen, others from Lac Tio.
[b]Discrepancies between these values and those in Table 1, most striking for this sample number, may relate both to measurement techniques and to use of different fragments of the same sample.

start to unblock by 570°C with tails persisting to 630°C [*Hargraves*, 1959a; *Hargraves and Burt*, 1967].

8.3. Thermomagnetic Curves

[48] Saturation magnetization was measured on AL23b, AL36b, and AL7b as a function of T from 30°C to 650°C. T_N, determined as the average from the heating and cooling curves, is ~610°C and 620°C ± 5°C for AL23b and AL36b, respectively. Sample AL7b from Lac Ellen deposit had a lower T_N of 600 ± 5°C. Curves are concave downward and nearly reversible, indicating little oxidation or reduction occurred during the experiment. The T_N are elevated relative to the hematite compositions determined by TEM.

8.4. Hysteresis Measurements

[49] Hysteresis measurements on low-susceptibility samples (<7 × 10^{-3} SI) with high T_N show a large paramagnetic component carried by the host ilmenite. After paramagnetic corrections, the room T saturation magnetization (M_s) ranges from 120 to 197 mA m^2/kg, and saturation remanence (M_{rs}) from 88 to 112 mA m^2/kg. M_{rs}/M_s ratios are high from 0.56 to 0.87. Coercive force (H_c) ranges from 119 to 170 mT, and coercivity of remanence (H_{cr}) from 130 to 213 mT resulting in H_{cr}/H_c ratios of 1.1 to 1.25.

[50] To check for anisotropy, a sample of AL36b was rotated every 10°, from 0 to 360°, for 36 hysteresis measurements. Two hysteresis loops measured in a 1.2 T field show a very strong anisotropy with a maximum and minimum "saturation" of Ms = 126 mA m^2/kg and Hc = 131 mT in the easy direction and Ms = 8.5 mA m^{2}kg and Hc = 713 mT in the hard direction. The latter is only a minor loop.

[51] To gain better understanding of the relationship between orientation of the lamellae and hysteresis properties, a very small polished slice of AL36b was measured in two directions. Traces of exsolution lamellae could be seen on the polished surface, though the exact three-dimensional orientation of lamellar planes could not be ascertained exactly. With the field nearly parallel to the traces, Hc = 137 mT. With the field nearly perpendicular to the traces, Hc = 343 mT (Figure 9). Thus, though the exact three-dimensional orientation of the lamellae in this chip is unknown, the measurements show that the harder direction is more nearly perpendicular to the lamellae than the softer.

[52] Because of strong magnetic anisotropy, orientation of hemo-ilmenite crystals and crystal aggregates with lattice-preferred orientation is a key factor in interpreting the data. A single hysteresis measurement will likely not be representative of a sample unless it consists of an aggregate of randomly oriented crystals. A sample with lattice-preferred orientation, or consisting of one, or a few crystals, results will depend on orientation of the experimental magnetic field relative to the crystals.

[53] Though most samples are not saturated in the 1.2 T fields used, it is useful to compare the saturation magnetization of pure hematite to these exsolved samples. Hematite has an M_s of ~2100 A/m [*Morrish*, 1994] or 404 mA m^2/kg. Allard Lake sample AL36b consists of 29.5% of the hematite phase, which means the hematite M_s would be reduced to 2100 A/m × 0.295 = 619.5 A/m. This would then be further reduced because 15% FeTiO$_3$ substitution weakens the magnetic interactions, thus 619.5 A/m × 0.91 = 563.7 A/m. This calculation takes into account that 15% FeTiO$_3$ substitution reduces the magnetization by only 9% due to the effect of Fe^{2+} in the ilmenite component. The M_s in these nonsaturated samples is 561–914 A/m using a mean density of 4640 kg/m^3. The 564 A/m for hematite versus 561–914 A/m for these samples, shows that the amount of magnetization is higher than be accounted for solely by CAF hematite lamellae. A defect moment, like that proposed for contact layers [*Robinson et al.*, 2002, 2004], could account for the increased magnetization. The amount of magnetization contributed by contact layers will be strongly affected by orientation of lamellae relative to the applied field at the time of magnetization, and the proportion of lamellae that are magnetically in-phase [*Robinson et al.*, 2004].

[54] Samples with susceptibility values >7 × 10^{-3} SI commonly contain magnetite that dominates hysteresis properties. Magnetite samples have Ms values up to 6.5 A m^2/kg, M_r/M_s values between 0.06 and 0.12, low coercivity values (Hc) between 4 and 12 mT and Hcr/Hc ratios up to 5.

[55] Shapes of Allard Lake hysteresis loops certainly reflect the mineralogy of "pure" hemo-ilmenite versus hemo-ilmenite with magnetite. Narrow loops are dominated by magnetite, whereas the "pure" hemo-ilmenite samples show a range in hysteresis parameters but all have Hc values above 100 mT. Because measured chips of sample material
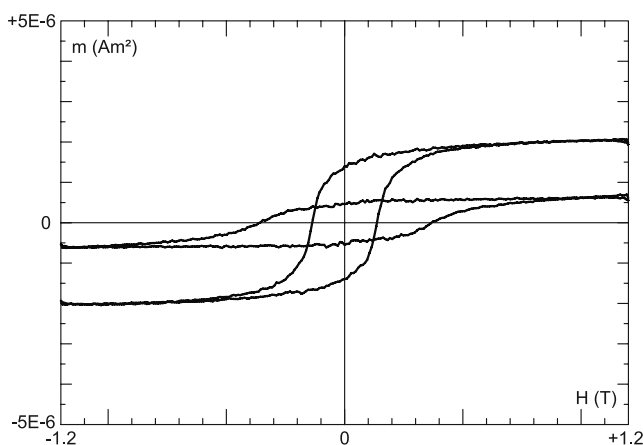

Figure 9. Two hysteresis loops for a sample chip of AL36b measured approximately parallel and perpendicular to the traces of the lamella. The results demonstrate the large anisotropy of hysteresis that can be measured in these exsolved samples.
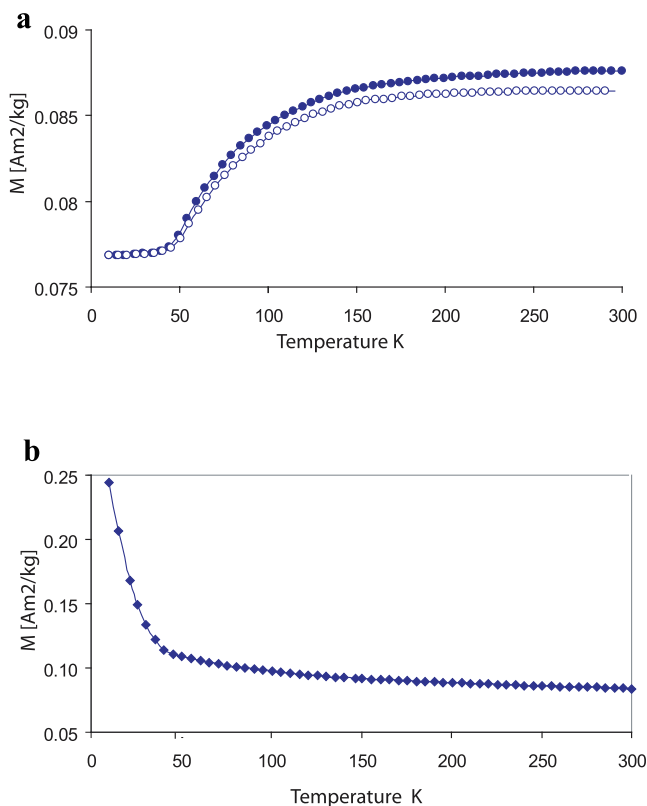
a

b

Figure 10. DC magnetization measurements (A136b) at low T. (a) A field of 2.5 T applied at 300 K. Then the sample was cooled in FFC to 10 K, with remanence measured every 5 K (solid symbols). Samples were warmed back to 300 K in ∼FFC (open symbols). (b) A 2.5 T field applied at 10 K. Then the sample was warmed in an approximately FFC and measured every 5 K in steps to 300 K.

were not single crystals, a range in all hysteresis parameters is expected, due to geometry and orientation of the crystals and their lamellae to the applied field, and to the size and abundance of lamellae.

8.5. DC Magnetization Measurements at Low Temperature

[56] Low-T measurements were made on a quantum design MPMS2 susceptometer on samples AL36b, AL20c, and AL7b. A 2.5 T field was applied at 300 K and samples were cooled in a zero field to 10 K with remanence measured every 5 K (Figure 10a). The Morin transition for hematite, and the Verwey transition for magnetite were absent in AL36b and AL7b. AL20c showed a loss in magnetization between 120 K and 110 K coincident with the Verwey transition for magnetite.

[57] Upon further cooling, from 100 K to 40 K, there is a distinct decrease in magnetization. At ∼40 K, the ilmenite host undergoes a transition from PM ilmenite to antiferromagnetic (AF) two-layer ordering, below which no further magnetization loss occurs. Samples were then warmed back to 300 K in near field free conditions. A rapid increase in magnetization begins at ∼45 K and continues until ∼140 K followed by a slow but small gain in magnetization with 99% recovery at 296 K. The increase above 45 K is the

result of the loss of magnetization in ilmenite, as it warms through the AF-PM transition. At low temperatures the ilmenite partially cancels magnetic moments of hematite lamellae and associated contact layers. The large recovery in magnetization shows that there is little energy lost in the system during the experiment, as would be expected if domain walls were moved, indicating that even the large hematite lamellae, 40 μm thick, behave as single domain particles. This behavior would also be expected if the ilmenite and hematite were exchange coupled through the interface.

[58] To look at ilmenite behavior below the AF-PM transition, a 2.5 T field was applied at 10 K, then the sample was warmed in a near-zero field and remanence measured in 5 K steps to 300 K (Figure 10b). A large loss in magnetization occurs by 25 K due to warming through a spin glass (SG) state to the AF state. Above ∼40 K, AF ilmenite converts to PM ilmenite, and over 80% of the magnetization is lost through this transition. Further warming to room temperature shows little change in the magnetization.

8.6. Frequency of Susceptibility Measurements at Low T

[59] Alternating current susceptibilities were measured using a quantum design MPMS2 susceptometer for samples AL36b, AL23, AL46, and AL7b for seven frequencies between 0.1 and 997 Hz, from 5 or 15 K to 300 K. The in-phase component of susceptibility is shown in Figure 11 for samples AL36b and Lac Ellen AL7b. The PM ilmenite contributes to an increase in susceptibility with cooling with a peak in the in-phase susceptibility (χ) at ∼44 K; $1/\chi$ shows an intercept at ∼43 K nearly coincident with the two-layer AF ordering T for the ilmenite component as determined by Mössbauer. The peak height is depressed with higher frequencies, and there is no shift in peak temperatures with the seven frequencies. Below 25 K, there is a very small dispersion in frequency measurements possibly related to interaction between two-layer AF ordering of ilmenite and adjacent layer ordering from the minor amounts of Fe^{3+} in the ilmenite. Below 25 K dispersion in the data is more evident and may correspond to a cluster spin glass structure, as described by *Ishikawa et al.* [1985]. When a small amount of Fe_2O_3 is added to $FeTiO_3$ the Fe^{3+} ions in the Ti^{4+} layers align the moments on the adjacent Fe^{2+} ions in parallel through adjacent layer ordering, resulting in formation of ferrimagnetic clusters which could behave "superparamagnetically" at temperatures near the spin glass transition [*Ishikawa et al.*, 1985]. In a $1/\chi$ plot, the slope of a paramagnetic material should intersect at the origin; an AF material should have a negative intersection, and ferrimagnetic material a positive intersection. From 300 K to ∼45 K, just above temperature of the AF two-layer ordering in ilmenite, $1/\chi$ plot has a positive intersection, indicating a ferrimagnetic component in the samples. This behavior could be due to the defect ferromagnetic substructure of contact layers associated with hematite-ilmenite interfaces. Both these samples have T_C well above 580°C.

8.7. Low-T Hysteresis Measurements

[60] Hysteresis properties were measured on samples AL36b, AL23b, and AL7b from 300 K down to 10 K to
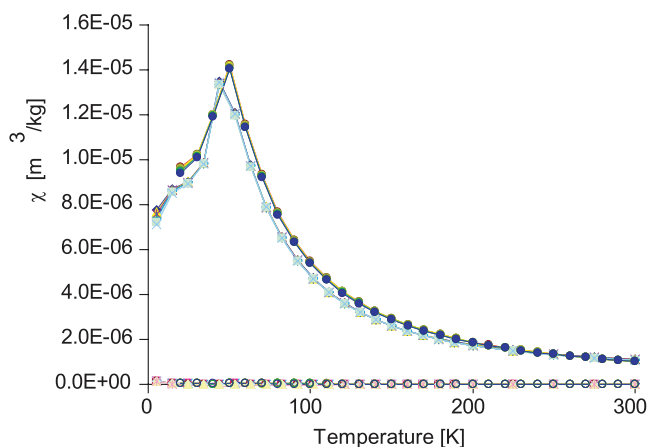
Figure 11. In-phase component of AC susceptibilities measured for seven frequencies between 0.2 and 997 Hz. AL36b (gray symbols) measured from 5 to 300 K and A17b (black symbols) from 20 to 300 K. Out-of-phase components are near zero for both samples.

study changes in magnetization below the Morin transition of hematite, and below the different ordering T of ilmenite, and to study effects of T on the lamellae and their interfaces. Though the discussion below is based on paramagnetic-corrected loops of AL36b, samples AL23b and AL7b show similar characteristics. Orientations of sample chips relative to applied field are not known, but the measurements were made in the same position for each sample from 300 to 10 K.

[61] Between 300 K and 200 K (Table 5) there is little change in the shape of the hysteresis loop, or in the M_{rs}/M_s and H_{cr}/H_c ratios. There is a general increase in H_c with decreasing temperature to 160 K. As expected there is no evidence for a Morin transition. M_s increases rapidly from 140 K down to 40 K where it reaches a maximum M_s of 2.56 A m^2/kg, $\sim$ the AF-ilmenite ordering T. The rapid increase in M_s is too large to be attributed only to paramagnetic ilmenite and may be due to the following:

[62] 1. An intralayer interaction between alternate hematite layers parallel to (0001), which are magnetically in-phase with the contact layers, spreads laterally, across lamellar boundaries at a high angle to (0001) into the adjacent Fe^{2+} in the surrounding ilmenite. This results in magnetic ordering of a small amount of adjacent ilmenite Fe^{2+} layers above the normal AF-ordering temperature, thus increasing the size of the magnetized volume.

[63] 2. The anisotropy keeping the spins in the basal plane weakens with decreasing temperature. The spins could be pulled into the direction of the applied field and would relax when the field is off, resulting in an increase in M_s but not in M_r.

[64] 3. Ilm 98 contains a small amount of Fe^{3+} in the Ti layers. The Fe amount in the Ti layers could be enhanced if there is FeTi disorder, although such disorder is unlikely due to the slow cooling history of the samples. Fe^{3+} in the Ti layers will cause development of small isolated SPM-like ferrimagnetic clusters by adjacent layer interaction that could increase M_s until lower temperature where the two-layer ordering sets.

[65] 4. Because there are multiple microstructures and phases; hematite and ilmenite, ilmenite lamellae in hematite, hematite lamellae in ilmenite and lamellar contact layers, the properties of each material behave differently with decreasing temperature. The present measurements cannot distinguish between the above options and future high-field measurements are planned.

[66] Below the Ilm T_N the M_s decreases to 2.0 A m^2/kg at 20 K. With lower T the M_s, increases again, to 2.2 A m^2/kg at 10 K, likely due to a spin glass produced by frustration of the small Fe clusters. Because of the clusters' extremely small size, their relaxation time may be too rapid to be measured by AC frequency and M_s measurements may be more sensitive to this transition.

[67] M_r behaves differently from M_s. At 80 K M_r has increased by 36%, whereas M_s has increased 5 times. At 10 K M_r is nearly doubled to 206 mA m^2/kg. Below the ilmenite AF ordering T, magnetic saturation properties are dominated by phase transitions of ilmenite. At and below 40 K, $\sim$ where ilmenite two-layer ordering is expected, the measurements are complicated by exchange interactions shown by shifted hysteresis loops of up to 40 mT. The exchange coupling leading to exchange bias is an effect between magnetic ions at the interface, and contact layers may play a role in this mechanism. This effect can be very large as demonstrate by the giant exchange bias of >1.3 T found in a titanohematite crystal with subunit cell size ilmenite lamellae, of <1 nm in diameter [*McEnroe et al.*, 2007].

9. Summary of Magnetic Properties

[68] The aim of this study was to understand the magnetic properties of a two-phase mixture of hematite and ilmenite, which has lamellar intergrowths from the micron down to the nanometer scale. On the TEM exsolution lamellae are observed as thin as the thickness of a single unit cell at $\sim$1.4 nm. The small lamellae are all still coherent with their hosts due to their small size and exhibit high strain shadows. The larger lamellae are incoherent with their hosts though they display also strong strain contrast. The misfit between the hematite and ilmenite is always the same and the formation of misfit dislocations of larger exsolutions is just

Table 5. Low-Temperature Hysteresis Properties of AL36b[a]

T, K	Mr	Ms	Mr/Ms	Hc	Hcr	Hcr/Hc
300	111	197	0.56	149	165	1.11
280	113	192	0.59	174	199	1.14
260	114	189	0.61	201	235	1.17
240	117	189	0.62	229	-	-
220	118	193	0.61	256	315	1.23
200	121	199	0.61	282	360	1.28
180	125	211	0.59	300	407	1.36
160	128	230	0.56	304	458	1.51
140	132	278	0.48	275	518	1.88
120	136	383	0.36	208	580	2.79
100	144	581	0.25	137	650	4.75
80	151	1093	0.14	75	735	9.8
60	157	2185	0.07	37	838	22.0
40	169	2564	0.07	42	883	21.0
20	195	2034	0.10	66	747	11.3
10	206	2090	0.10	70	616	8.8

[a]Mr and Ms in mA m^2/kg; Hc and Hcr in mT.

a consequence of the larger size of lamellae. The extent to which lamellar size and lattice strain influence magnetic properties, is an area for future research.

[69] The measured properties show that hematite lamellae of all sizes appear to be magnetically stable, at least within the timescale of and the amount detectable with the applied techniques. On the basis of the low-T phase diagram (Figure 7), and the Ilm 98 compositions determined here, the host ilmenite and ilmenite lamellae should not show SPM-like behavior, as occurs in slightly more Fe-rich samples, but do appear to be involved in development of a cluster SG at ∼20 K.

[70] Allard Lake samples without magnetite exhibit very high coercivity; nearly complete resistance to AF demagnetization to 120 mT, and large NRM values. Strong anisotropy was demonstrated in the rotational hysteresis measurements, with a magnetization 15 times higher in the easy direction than in the hard direction. In the hard direction, only a minor loop could be measured with a coercivity of >700 mT. Samples without magnetite have T_N above 600°C and unblocking between 610 and 620°C. Shifted hysteresis loops show an exchange bias of 40 mT due to ilmenite interaction with contact layers or to spin glass. The large recovery in magnetization when the sample is cooled to 10 K and then warmed in near-field-free conditions is remarkable, and shows that this type of magnetization is very stable at low T.

[71] The complexity of low-T phases in the ilmenite-rich side of the diagram is evident, with the changes in magnetic structures from PM → AF → CSG. The large increase in magnetization in sample 36b below 20 K is likely due to the additional magnetization caused by frustrations between adjacent and two-layer ordering, which produces a spin glass.

10. Implications for Crustal Magnetism of Earth and Other Planets

10.1. Role of Exsolved Rhombohedral Oxides in Planetary Magnetism

[72] In this paper we attempted to understand the nature of magnetism in a mineral system that can produce large NRMs that are also very stable over geologic time. Looking at settings on Earth that produce large remanent anomalies helps to predict the geology, minerals, and structural settings on Mars. At or near the surface on Earth, a rock that contains minor amounts of hemo-ilmenite or ilmeno-hematite with microstructures like those in the Allard Lake samples will likely create remanence-dominated anomalies, even with minor amounts magnetite, because of the strong and stable NRM, which in turn creates very large Q values. Although igneous and metamorphic rock compositions oxidized enough to contain significant volumes of hemo-ilmenite and ilmenohematite are not predominant on earth, they are nevertheless voluminous in extensive regions, including but not limited to Proterozoic anorthosite provinces and granulite terranes in Australia, in the Baltic Shield, and in the Grenville Province of eastern North America, typified by the region around Allard Lake, Quebec.

[73] Remanence-dominated anomalies are most easily recognized where the anomalies are negative, with a

remanent vector at a high angle to the present field. Where the remanence is oriented quasi-parallel to the present field, the anomaly can be attributed incorrectly to the induced magnetic field, if no magnetic property data or structural constraints are available [*Schmidt et al.*, 2007]. The first author and coworkers have studied numerous localities on Earth with minerals that produce remanence-dominated anomalies, varying in amplitude and scale, but all dominated by the ancient vector that was acquired ∼1 billion years ago. There are pertinent questions to ask about the observed relationships during ongoing research. Why do the magnitudes of the NRM vectors related to anomalies vary so much for rocks where the amount of oxide is similar? Why are the anomalies an order of magnitude higher in some settings than in others?

10.2. Some Key Properties of Exsolved Rhombohedral Oxides

[74] Key features of the lamellar magnetism of rhombohedral oxides lie in high coercivity and strong magnetization at elevated T equal to or higher than the Curie T of magnetite at 580°C, which can lose a significant amount of remanence well below its Curie T. The special properties of Allard Lake hemo-ilmenite may arise from the relatively hematite-rich bulk composition at Ilm 72.5, allowing coarse exsolution to begin at high T, and this coarseness allowed a more complete exsolution, so that ultimately much of the ilmenite reached a composition close to Ilm 98. Contact layers at hematite-ilmenite interfaces may help stabilize the magnetism so that a component of it may persist with a large magnetization over long time periods.

[75] Ilm 98 shows little or no superparamagnetism and the magnetization acquired at low T is that of nearly pure ilmenite. However, a reduction of T_N from 57 to ∼43 K shows the importance of Fe_2O_3 (and $MgTiO_3$?) substitution in influencing magnetic properties. Below 20 K near end-member ilmenite can be very magnetic, where minor Fe^{3+} substitution appears to cause development of a cluster spin glass. With or without lamellae, ilmenite at low temperature with its high magnetization and strong anisotropy presents interesting possibilities for the magnetization of cold planets, such as those that lost their atmospheres. Further work is needed on defining the ilmenite-hematite phase diagram, particularly the magnetic transitions at low temperature. With planned future exploration of cold planets, understanding ilmenite-hematite solid solution behavior at different temperatures will become important. On the Moon where a geikielite-rich ilmenite is an important oxide [*Shearer et al.*, 2006] understanding the temperature-dependent magnetic properties of an Mg-substituted ilmenite could be beneficial for exploration purposes.

10.3. Magnetism at Depth in Planetary Crusts

[76] To what extent will exsolved rhombohedral oxides at depth in planetary crusts contribute to magnetic anomalies? Demagnetization T of many Allard Lake samples are above that of magnetite at 1 atm; however, the Curie temperature of magnetite increases with pressure ∼2.3°C/kbar [*Schult*, 1970]. Can rhombohedral oxide mineralogy be stable at higher temperature and contribute a remanent component to magnetic anomalies from deeper and warmer crust, where

previously anomalies were assumed to be purely induced and due to magnetite, with its much weaker coercivity? The pressure effect on a miscibility gap is usually to widen it, resulting in greater thermal stability of the assemblage consisting of host and lamellae. For the hematite-ilmenite system, this is a matter of some uncertainty, partly because of the unusual negative volume of mixing in the series [*Harrison et al.*, 2000b] and because the pressure effect on the hematite magnetization temperature is simply unknown. However, recent measurements of ilmenite cation-ordering temperature [*Harrison et al.*, 2006] suggest an increase of about 100° with 10 kbar pressure, likely coupled with a widening of the hematite-ilmenite two-phase field at high temperature. In piston cylinder experiments at 580°C and 10 kbar results showed that hematite exsolution lamellae in ilmenite host are stable, and actually coarsen [*McEnroe et al.*, 2004b]. The high NRMs, 12 to 120 A/m, coupled with high coercivity and thermal stability makes this mineralogy a likely source for anomalies at depth in the crust. Depending on composition, exsolution lamellae could contribute a substantial magnetic signal at depths below the Curie isotherm for magnetite, where both the induced and remanent magnetic signal for magnetite is lost. With the upcoming launch of the new SWARM satellites, more work is needed on effects of pressure and temperature on the magnetization of ilmenite-hematite intergrowths, and a greater understanding of phase petrology is necessary to predict which rock types and under what conditions this assemblage will be stable.

10.4. Exsolved Rhombohedral Oxides as a Cause of Magnetic Anomalies on Mars

[77] Rocks containing nanoscale ilmenite-hematite intergrowths are candidates for the large remanent magnetic anomalies on Mars [*McEnroe et al.*, 2001a, 2001b, 2002, 2004a, 2004b, 2004c], which lost its magnetic field early in its history. The Martian anomalies require very large rock volumes over areas of hundreds of km^2 and extending 20–30 km deep [*Acuña et al.*, 1999; *Connerney et al.*, 1999]. Predicted NRMs are large, ~20 A/m or more, and the rocks creating the anomalies are considered to be >4 Ga old [*Langlais et al.*, 2004]. To retain magnetization for such a time span, the material likely needs a relatively high coercivity. On Earth, many anomalies have a large component of the present-day field, because the NRM decays due to relaxation, creating a viscous remanent magnetization, generally attributed to a low-coercivity phase such as magnetite, also having a higher susceptibility and thus a higher inducing factor. On Earth, for the NRM to dominate an anomaly, it must be much stronger than the inducing contribution. On Mars, there is only a minor "inducing" component from the residual crust field, because Mars has long lacked an internal magnetic field. The Allard Lake hemo-ilmenite deposit is a worthy candidate to study in detail, because the anomaly has been present in a harsher magnetic environment than occurred on Mars, due to hundreds of Earth magnetic field reversals since the ore acquired its magnetization.

References

Acuña, M. H., et al. (1999), Global distribution of crustal magnetization discovered by the Mars Global Surveyor MAG/ER Experiment, *Science*, *284*, 790–793.

Arai, M., and Y. Ishikawa (1985), A new oxide spin glass system of (1-x) FeTiO$_3$ – x Fe$_2$O$_3$. III. Neutron scattering studies of magnetization processes in a cluster type spin glass of 90 FeTiO$_3$-10Fe$_2$O$_3$, *J. Phys. Soc. Jpn.*, *54*, 795–802.

Arai, M., Y. Ishikawa, N. Saito, and H. Takei (1985a), A new oxide spin glass system of (1-x) FeTiO$_3$ – x Fe$_2$O$_3$. II. Neutron scattering studies of a cluster type spin glass of 90 FeTiO$_3$-10Fe$_2$O$_3$, *J. Phys. Soc. Jpn.*, *54*, 781–794.

Arai, M., Y. Ishikawa, and H. Takei (1985b), A new oxide spin glass system of (1-x) FeTiO$_3$ – x Fe$_2$O$_3$. IV. Neutron scattering studies on a re-entrant spin glass of 79FeTiO$_3$-21Fe$_2$O$_3$ single crystal, *J. Phys. Soc. Jpn.*, *54*, 2279–2286.

Ashwal, L. D. (1993), *Anorthosites*, 422 pp., Springer, Berlin, Germany.

Bourret, W. (1949), Aeromagnetic survey of the Allard Lake district, Quebec, *Econ. Geol.*, 732–740.

Brown, N. E., A. Navrotsky, G. L. Nord Jr., and S. K. Banerjee (1993), Hematite-ilmenite (Fe$_2$O$_3$-FeTiO$_3$) solid solutions: Determinations of Fe-Ti order from magnetic properties, *Am. Mineral.*, *78*, 941–951.

Burton, B. P. (1982), Thermodynamic analysis of the systems CaCO$_3$-MgCO$_3$, α-Fe$_2$O$_3$ and Fe$_2$O$_3$-FeTiO$_3$, Ph.D. thesis, pp. 117–118, State Univ. of N. Y. at Stony Brook, Stony Brook.

Burton, B. P. (1984), Thermodynamic analysis of the system Fe$_2$O$_3$-FeTiO$_3$, *Phys. Chem. Miner.*, *11*, 132–139.

Burton, B. P. (1985), Theoretical analysis of chemical and magnetic ordering in the system Fe$_2$O$_3$-FeTiO$_3$, *Am. Mineral.*, *70*, 1027–1035.

Burton, B. P. (1991), Interplay of chemical and magnetic ordering, in *Oxide Minerals*, *Rev. Mineral.*, vol. 25, edited by D. H. Lindsley, pp. 303–321, Mineral. Soc. of Am., Washington, D. C.

Burton, B., and R. Kikuchi (1984), Thermodynamic analysis of the system CaCO$_3$-MgCO$_3$ in the tetrahedron approximation of the cluster variation method, *Am. Mineral.*, *69*, 165–175.

Carmichael, C. M. (1959), Remanent magnetization of the Allard lake ilmenites, *Nature*, *183*, 1239–1241.

Carmichael, C. M. (1961), The magnetic properties of ilmenite-hematite crystals, *Proc. R. Soc. London, Ser. A*, *243*, 508–530.

Carmichael, C. M. (1964), The magnetization of a rock containing magnetite and hemo-ilmenite, *Geophysics*, *26*, 87–92.

Connerney, J. E. P., M. H. Acuña, P. Wasilewski, N. F. Ness, H. Rème, C. Mazelle, D. Vignes, R. P. Lin, D. L. Mitchell, and P. Cloutier (1999), Magnetic lineations in the ancient crust of Mars, *Science*, *284*, 794–798.

Frandsen, C., S. Mørup, S. A. McEnroe, P. Robinson, and F. Langenhorst (2007), Magnetic properties of hemo-ilmenite: Insight from low-velocity and high-field Mössbauer spectroscopy, *Geophys. Res. Lett.*, *34*, L07306, doi:10.1029/2006GL029063. (Correction, *Geophys. Res. Lett.*, *34*, L09317, doi:10.1029/2007GL030387.)

Ghiorso, M. S. (1997), Thermodynamic analysis of the effect of magnetic ordering on miscibility gaps in the FeTi cubic and rhombohedral oxide minerals and the FeTi oxide geothermometer, *Phys. Chem. Miner.*, *25*, 28–38.

Hammond, P. (1952), Allard lake ilmenite deposits, *Econ. Geol.*, *47*, 636–649.

Hargraves, R. B. (1959a), Magnetic anisotropy and remanent magnetization in hemo-ilmenite from ore deposits of Allard Lake, Quebec, *J. Geophys. Res.*, *64*, 1565–1573.

Hargraves, R. B. (1959b), Petrology of the Allard Lake anorthosite suite, and paleomagnetism of the ilmenite deposits, Doctoral thesis, 193 pp., Princeton Univ., Princeton, N. J.

Hargraves, R. B. (1962), Petrology of the Allard Lake anorthosite suite, Quebec, in *Petrologic studies: A volume in honor of A. F. Buddington*, edited by A. E. J. Engel et al., pp. 163–189, Geol. Soc. of Am., Boulder, Colo.

Hargraves, R. B., and D. M. Burt (1967), Paleomagnetism of the Allard Lake anorthosite suite, *Can. J. Earth Sci.*, *4*, 357–369.

Harrison, R. J. (2000), Magnetic transition in minerals, in *Transformation Processes in Minerals*, *Rev. Mineral.*, vol. 39, edited by S. A. T. Redfern and M. A. Carpenter, pp. 175–202, Mineral. Soc. of Am., Washington, D. C.

Harrison, R. J. (2006), Microstructure and magnetism in the ilmenite-hematite solid solution: a Monte Carlo simulation study, *Am. Mineral.*, *91*, 1006–1023.

Harrison, R. J., and U. Becker (2001), Magnetic ordering in solid solutions, in *Solid Solutions in Silicate and Oxide Systems*, *Notes Mineral.*, vol. 3, edited by C. A. Geiger, pp. 349–383, Eur. Mineral. Union, Vienna, Austria.

Harrison, R. J., and S. A. T. Redfern (2001), Short- and long-range ordering in the ilmenite-hematite solid solution, *Phys. Chem. Miner.*, *28*, 399–412.

Harrison, R. J., U. Becker, and S. A. T. Redfern (2000a), Thermodynamics of the R-3 to R-3c phase transition in the ilmenite-hematite solid solution, *Am. Mineral.*, *85*, 1694–1705.

Harrison, R. J., S. A. T. Redfern, and R. I. Smith (2000b), In-situ study of the R3 to R3c phase transition in the ilmenite-hematite solid solution using time-of-flight neutron powder diffraction, *Am. Mineral.*, *85*, 194–205.

Harrison, R. J., H. J. Stone, and S. A. T. Redfern (2006), Pressure dependence of Fe-Ti order in the ilmenite-hematite solid solution: implications for the origin of lower crustal magnetization, *Phys. Earth Planet. Inter.*, *154*, 266–275.

Ishikawa, Y., and S. Akimoto (1957), Magnetic properties of the $FeTiO_3$-Fe_2O_3 solid solution series, *J. Phys. Soc. Jpn.*, *12*, 1083–1098.

Ishikawa, Y., N. Saito, M. Arai, Y. Watanabe, and H. Takei (1985), A new oxide spin glass system of $(1-x)$ $FeTiO_3 - x$ Fe_2O_3. I. Magnetic properties, *J Phys. Soc. Jpn.*, *54*, 312–325.

Kasama, T., S. A. McEnroe, N. Ozaki, T. Kogure, and A. Putnis (2004), Effects of nanoscale exsolution in hematite-ilmenite on the acquisition of stable natural remanent magnetization, *Earth Planet. Sci. Lett.*, *224*, 461–475.

Kletetschka, G., P. J. Wasilewski, and P. T. Taylor (2002), The role of hematite-ilmenite solid solution in the production of magnetic anomalies in ground- and satellite-based data, *Tectonophysics*, *347*, 167–177.

Langenhorst, F., P. Joreau, and J. C. Doukhan (1995), Thermal and shock metamorphism of the Tenham meteorite: A TEM examination, *Geochim. Cosmochim. Acta*, *59*, 1835–1845.

Langlais, B., M. E. Purucker, and M. Mandea (2004), Crustal magnetic field of Mars, *J. Geophys. Res.*, *109*, E02008, doi:10.1029/2003JE002048.

Larson, A. C., and R. B. von Dreele (1994), GSAS: General Structure Analysis System, Document LAUR, pp. 86–748, Los Alamos Natl. Lab., Los Alamos, N. M.

McEnroe, S. A., and L. L. Brown (2000), A closer look at remanence-dominated anomalies: Rock-magnetic properties and magnetic mineralogy of the Russell Belt microcline-sillmanite gneisses, northwest Adirondacks Mountains, New York, *J. Geophys. Res.*, *105*, 16,437–16,456.

McEnroe, S. A., R. J. Harrison, P. Robinson, U. Golla, and M. J. Jercinovic (2001a), The effect of fine-scale microstructures in titanohematite on the acquisition and stability of NRM in granulite facies metamorphic rocks from southwest Sweden, *J. Geophys. Res.*, *106*, 30,523–30,546.

McEnroe, S. A., P. Robinson, and P. T. Panish (2001b), Aeromagnetic anomalies, magnetic petrology and rock magnetism of hemo-ilmenite- and magnetite-rich cumulates from the Sokndal Region, South Rogaland, Norway, *Am. Mineral.*, *86*, 1447–1468.

McEnroe, S. A., R. J. Harrison, P. Robinson, and F. Langhorst (2002), Nanoscale haematite-ilmenite lamellae in massive ilmenite rock: An example of lamellar magnetism with implications for planetary magnetic anomalies, *Geophys. J. Int.*, *151*(3), 890–912.

McEnroe, S. A., L. L. Brown, and P. Robinson (2004a), Earth analog for Martian magnetic anomalies: Remanence properties of hemo-ilmenite norites in the Bjerkreim-Sokndal Intrusion, Rogaland, Norway, *J. Appl. Geophys.*, *56*(3), 195–212.

McEnroe, S. A., F. Langenhorst, P. Robinson, G. D. Bromiley, and C. S. J. Shaw (2004b), What's magnetic in the lower Crust?, *Earth Planet Sci. Lett.*, *226*, 175–192.

McEnroe, S. A., J. R. Skilbrei, P. Robinson, F. Heidelbach, F. Langenhorst, and L. L. Brown (2004c), Magnetic anomalies, layered intrusions and Mars, *Geophys. Res. Lett.*, *31*, L19601, doi:10.1029/2004GL020640.

McEnroe, S. A., R. J. Harrison, P. Robinson, F. Langenhorst, T. Kasama, A. Putnis, M. Jackson, A. Hirt, L. L. Brown, and U. Golla-Schindler (2005), Lamellar magnetism: Effects of interface versus exchange interactions of nanoscale exsolutions in the ilmenite-hematite system, *J. Phys. Conf. Ser.*, *17*, 154–167.

McEnroe, S. A., B. Carter-Stiglitz, R. J. Harrison, P. Robinson, K. Fabian, and C. McCammon (2007), Magnetic exchange bias of more than 1 Tesla in a natural mineral intergrowth, *Nat. Nanotechnol.*, *2*, 631–634, doi:10.1038/nnano.2007.292.

Morrish, A. H. (1994), *Canted Antiferromagnetism: Hematite*, World Sci., Singapore.

Robinson, P. (1980), The composition space of terrestrial pyroxenes—Internal and external limits, in *Pyroxenes*, *Rev. Mineral.*, vol. 7, edited by C. T. Prewitt, pp. 419–494, Mineral. Soc. of Am., Washington, D. C.

Robinson, P., R. J. Harrison, S. A. McEnroe, and R. Hargraves (2002), Lamellar magnetism in the hematite-ilmenite series as an explanation for strong remanent magnetization, *Nature*, *418*, 517–520.

Robinson, P., R. J. Harrison, S. A. McEnroe, and R. Hargraves (2004), Nature and origin of lamellar magnetism in the hematite-ilmenite series, *Am. Mineral.*, *89*, 725–747.

Robinson, P., F. Heidelbach, A. M. Hirt, S. A. McEnroe, and L. L. Brown (2006), Crystallographic-magnetic correlations in single-crystal hemo-ilmenite: new evidence for lamellar magnetism, *Geophys. J. Int.*, *165*, 17–31.

Schmidt, P. W., S. A. McEnroe, D. A. Clark, and P. Robinson (2007), Magnetic properties and potential field modeling of the Peculiar Knob metamorphosed iron formation, South Australia: An analog for the source of the intense Martian magnetic anomalies?, *J. Geophys. Res.*, *112*, B03102, doi:10.1029/2006JB004495.

Schult, A. (1970), Effect of pressure on the Curie temperature of titano-magnetites $[(1-x)Fe_3O4-xTi\ Fe_2O_4]$, *Earth Planet. Sci. Lett.*, *10*, 81–86.

Shearer, C. K., et al. (2006), Thermal and magmatic evolution of the Moon, in *New Views of the Moon*, *Rev. Mineral.*, vol. 60, edited by B. L. Jolliff et al., pp. 365–518, Mineral. Soc. of Am., Washington, D. C.

Stanaway, K. J. (2005), Four world titanium mining provinces, paper presented at 2005 Heavy Minerals Conference, Soc. for Min., Metall., and Explor., Inc., Ponte Vedra Beach, Fla., 16–19 Oct.

Toby, B. H. (2001), EXPGUI, a graphical user interface for GSAS, *J. Appl. Crystallogr.*, *34*, 210–213.

Waychunas, G. A. (1991), Crystal chemistry of oxides and hydroxides, *Rev. Mineral.*, *25*, 11–68.

————————————

T. Boffa Ballaran and M. P. Terry, Bayerisches Geoinstitut, Universität Bayreuth, D-95440 Bayreuth, Germany.

F. Langenhorst, Institute of Geosciences, Friedrich-Schiller-University Jena, Jena, Burgweg 11, D-07749 Jena, Germany.

C. Frandsen, Department of Physics, Technical University of Denmark, DK-2800 Kongens Lyngby, Denmark.

S. A. McEnroe and P. Robinson, Geological Survey of Norway, N-7491, Trondheim, Norway. (suzanne.mcenroe@ngu.no)